

Supplementary Information

Electrical Unfolding of Cytochrome c During Translocation Through a Nanopore Constriction

Prabhat Tripathi^a, Abdelkrim Benabbas^a, Behzad Mehrafrooz^b, Hirohito Yamazaki^a,
Aleksi Aksimentiev^{b,c}, Paul M. Champion^{a,d,1}, and Meni Wanunu^{a,d,1}

^aDepartment of Physics, Northeastern University, Boston, MA, 02115; ^bCenter for Biophysics and Quantitative Biology, University of Illinois at Urbana-Champaign, Urbana, IL 61801; ^cDepartment of Physics and Beckman Institute for Advanced Science and Technology, University of Illinois at Urbana-Champaign, Urbana, IL 61801; ^dCenter for Interdisciplinary Research on Complex Systems, Northeastern University, Boston, MA 02115

Table of Contents:

This document contains following sections:

1. Materials and methods.
2. Sequence and gel electrophoresis of cyt c used in our experiments.
3. Surface charge measurements of a high-stress SiN pore.
4. Open-pore conductance for different pore diameters.
5. Electric field and dipole orientations.
6. Representative current traces for cyt c using a 2.5 nm pore at different voltages.
7. Two-state model for $\Delta I/I_o$ vs. E_{app} in the dynamical unfolding limit (for 2.0 nm pore).
8. Representative current traces for cyt c using different pore diameters at -100 mV.
9. Representative current traces for cyt c using 2.0 nm and 1.5 nm diameter pores.
10. Representative $\Delta I/I_o$ histograms and fraction of events with level ii for cyt c using a 2.0 nm pore.
11. MD simulation methods and data for a 1.5 nm pore.
12. Distributions of $\Delta I/I_o$ as a function of voltage for cyt c using a 3.0 nm pore.
13. Experiments in presence of Gdm-Cl (denaturation data).
14. Multicomponent Gaussian fits to the $\Delta I/I_o$ distributions for cyt c using a 2.5 nm pore.
15. Three-state model for $\Delta I/I_o$ vs. E_{app} in the dynamical unfolding limit (analysis for 2.5 nm pore).
16. Representative histograms of $\tau_{residence}$ for a 2.5 nm pore at higher electric fields.
17. Translocation kinetics and fast exchange of folding/unfolding α -helices (2.5 nm pore).
18. Extraction of zero-field translocation barrier of U state for a 2.0 nm pore ($L = 4.1$ nm).
19. Extraction of zero-field translocation barriers of M and U states for a 2.5 nm pore ($L = 3.4$ nm).
20. Open pore current vs voltage measurements for different pore diameters.
21. Scenarios for level ii event lifetime distributions in the 2.0 nm pore

1. Materials and methods (Experimental)

We used ultrathin high-stress SiN (250 MPa) membranes supported by a Si chip as substrates for nanopore fabrication(1-3). Nanopores were cleaned in hot piranha (2:1 H₂SO₄ / H₂O₂) for 30 minutes, followed by hot deionized water, before each experiment. After cleaning, nanopore chips were assembled in a custom flow cell equipped with Ag/AgCl electrodes, and a quick-curing silicone elastomer was applied between the chip and the cell to seal the device and thereby reduce the noise by minimizing the chip capacitance.

The purity of equine heart cyt c (Sigma Aldrich C2506) was confirmed by SDS PAGE gel electrophoresis (Fig. S1(ii)). All experiments were carried out at ambient temperature. The apparent electric field (E_{app}) inside the pore were obtained by ratio of applied electric potential in *trans* chamber and length of the pore and was used to interpret the data.

SDS-PAGE gel electrophoresis:

Preparation of gel: We added 4.9 ml of deionized water to a 50 ml cylindrical tube, then added 6 ml of 30% acrylamide mix, 3.8 ml of 1.5M tris (pH 8.8), 0.15 ml of 10% SDS, 0.15 ml of 10% ammonium persulfate, 0.006 ml of TEMED. The resultant solution was shaken and added to the gel-glass-plate. A comb was inserted to generate the well structures, and a 30 minute waiting time allowed polymerization of the gel.

10X running buffer: We dissolved 30.0 g of tris base, 144.0 g of glycine, and 10 g of SDS in 1000 ml of H₂O. The pH of the buffer was observed to be 8.3 without any adjustment. The resultant solution was stored at room temperature and diluted to 1X before use for gel electrophoresis experiments.

Running the gel: We loaded the gel-glass-plate in a vertical electrophoresis cell, and then added 1X running buffer. We heated the cyt c solution (1 mg/ml) at 95°C for 5 minutes in heat block and then 10 μL of cyt c was added to one well, alongside another well that was loaded a molecular weight marker. Voltage was set to a fixed value of 150 V, and the gel was allowed to run for 45 minutes.

Electrical detection and data acquisition.

The ionic current through nanopores was measured using an Axopatch 200B amplifier (Molecular Devices) and low-pass filtered to indicated bandwidth using the internal Bessel filter of the Axopatch. Data points were digitized and sampled at 250 kHz sample rates on a National Instruments DAQ card using custom LabVIEW software. For the 5.5 nm pore we have performed high-bandwidth measurements of ionic current using a Chimera instruments VC100 amplifier (4). Data were processed and events were detected using Pythion (<https://github.com/rhenley/Pythion/>) and multilevel events were detected using a custom algorithmic procedure in Igor Pro software (as described below).

Algorithms for multilevel detection:

The algorithms developed here for multilevel detection in a typical nanopore trace fall under the umbrella of change point detection techniques in a time series. Here, we are mainly concerned with changes of the mean of the distribution; and below we briefly describe two algorithms that that have been used throughout this paper:

(a) Two sliding windows (TSW) algorithm:

This method uses two sliding consecutive windows each with n datapoints all having the same y value corresponding to the mean of the trace within the window; which is denoted w_1 for the first window and w_2 for the second. The user chooses 2 datapoints on a continuous segment of baseline bn_1 and bn_2 . These two data points are used by the program to calculate the mean and the standard deviation of the baseline denoted as *baseline* and σ , respectively. We then define a threshold, th , for change point detection from baseline to event and vice versa. th is defined as: $th = n_{th}\sigma$; with n_{th} typically varies from 4 to 10. In most cases biomolecules rotate and change conformation at the mouth of or within the pore. These rotational and conformational motions superimpose with the intrinsic noise of the baseline and increase the apparent noise of the levels of an event. To deal with this situation we define a level threshold, th_l , that is typically larger than th .

The two windows slide and scan the trace with steps of n datapoints using a for loop and at each step we check for the following conditions:

- (i) If $(baseline - w_1 \leq th) \text{ and } (baseline - w_2 > th)$: this indicates the end of baseline, start of an event and start of the first level of the event. The segment of the baseline that has ended is fitted with the mean of its datapoints.
- (ii) Elseif $(baseline - w_1 > th) \text{ and } (baseline - w_2 > th) \text{ and } (abs(w_1 - w_2) > th_l)$: this indicates the end of a level and the start of another within an event. The segment of the level that has ended is fitted with the mean of its datapoints.
- (iii) Elseif $(baseline - w_1 > th) \text{ and } (baseline - w_2 \leq th)$: this indicates the end of an event and its last level and the start of the baseline. The segment of the last level that has ended is fitted with the mean of its datapoints.

The levels are indexed as (i, j) , where i is the index of the event and j is the index of the level within the event.

(b) Extending window and sliding window (EWSW) algorithm:

This method uses two consecutive windows, an extending window (w_1) which represents the cumulative mean of all the datapoint after the last change point and a sliding window (w_2) with n datapoints all having the same y value corresponding to the mean of the trace within the window. The steps of this algorithm are the same as the TSW algorithm with the only exception is the change of the meaning of w_1 .

To speed up the calculation we do not calculate the cumulative mean each time by taking the average of the previous datapoint and we use the following trick instead: at each step k the cumulative sum *cusum* and cumulative number of points *cuN* are updated by calculating them recursively using the following formulas:

$$\begin{aligned} cusum_k &= cusum_{k-1} + n(w_2)_{k-1} \\ cuN_k &= cuN_{k-1} + n \\ (w_1)_k &= cusum_k / cuN_k \end{aligned}$$

Both techniques fit multilevel traces well; however, in some cases the EWSW algorithm performs better than TSW. Therefore, all the traces in this paper are fit using EWSW algorithm. More details about the performance of these algorithms will be discussed in a separate paper.

2. Sequence and gel electrophoresis of cyt c used in our experiments

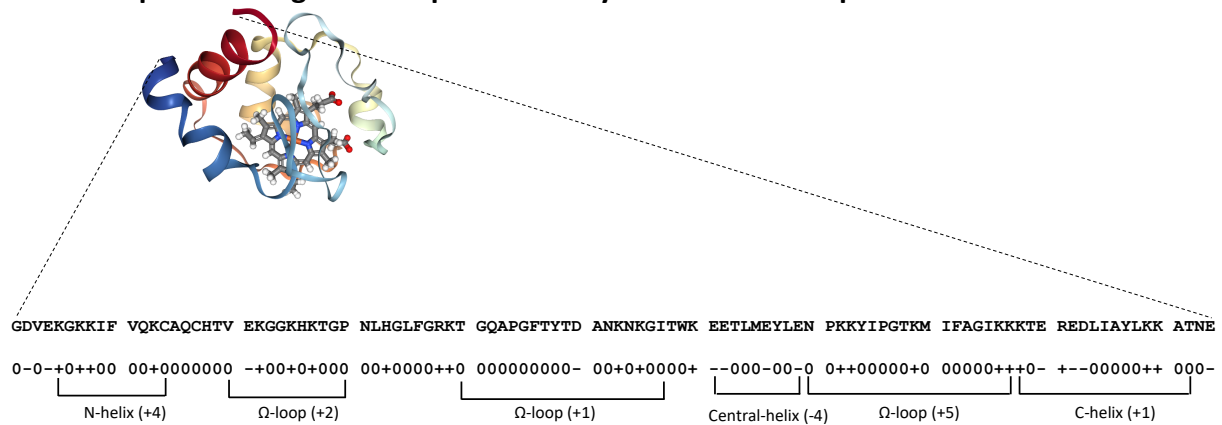


Figure S1 (i) Sequence of equine heart cyt c used in the experiments and a segmental representation of the charge distributions.

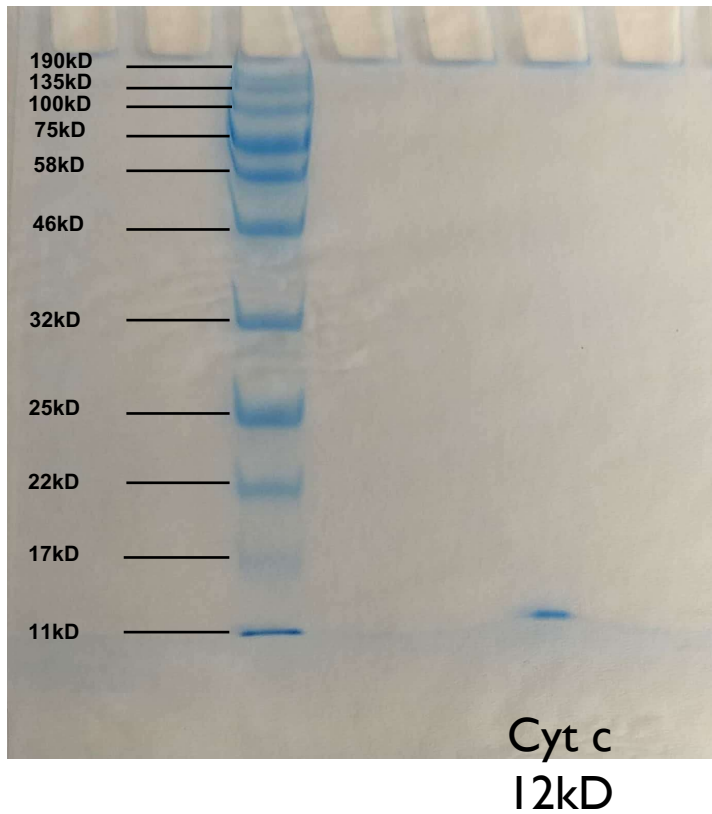


Figure S1(ii) Gel electrophoresis of cyt c (equine heart) used in the experiments. A clear single band near 12 kD indicates the purity of the sample, and confirms that no covalent (e.g., disulfide-bridged) dimers are formed.

3. Surface charge measurements of a high-stress SiN nanopore

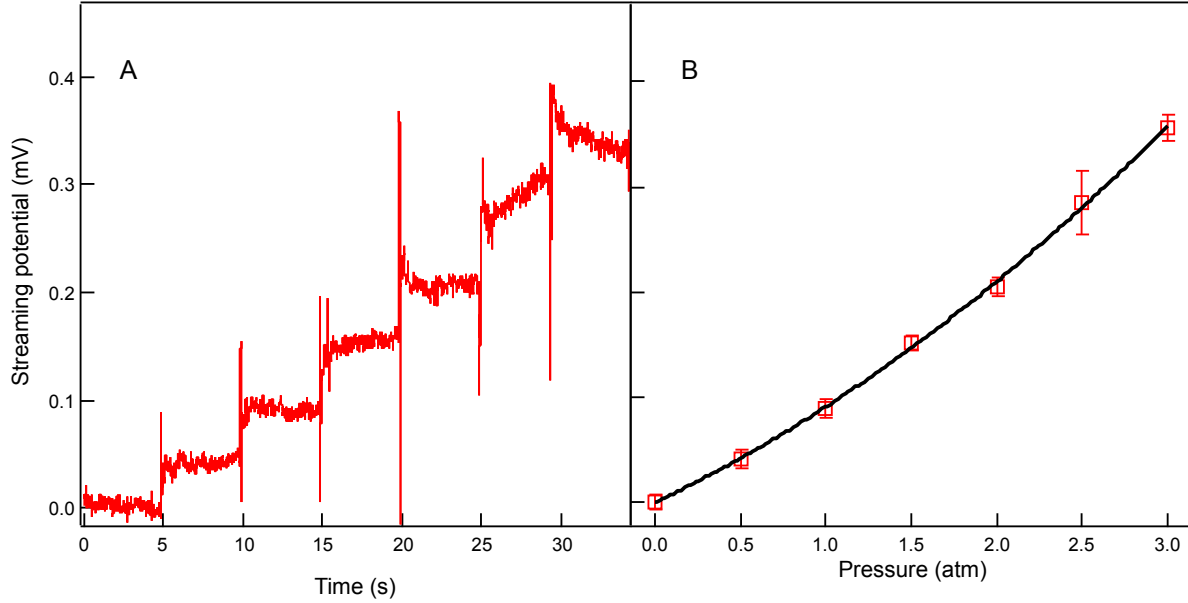


Figure S2. Example surface charge measurement of a high-stress (250 MPa) SiN pore. A) Streaming potential current trace of 6.1 nm pore in 0.4 M KCl, 10 mM Tris, 1 mM EDTA pH 7.8. Using automated pneumatic pressure controller, streaming potential was measured by applying 0.5 atm increments every 5 seconds. B) Streaming potential vs. pressure. The black solid curve in panel B represents the fit with a quadratic function $a x^2 + b x + c$, $a = 0.014$, $b = 0.077$, $c = -0.001$. Error bars in panel B represent the \pm standard deviation from the mean streaming potential data.

Fig. S2(A) shows 30-sec streaming potential trace of 6.1 nm diameter SiN pore with increment of 0.5 atm in 0.4 M KCl, 10 mM Tris, 1 mM EDTA, pH 7.8. The air pressure is applying on cis chamber using the automated pneumatic pressure scanner. The average streaming potential as a function of applied pressure is plotted in Fig. S2(B). As presented in our previous work (5, 6), the zeta potential is expressed as the following equation;

$$\zeta = \frac{\eta \kappa}{\varepsilon} \frac{L}{L + \pi a / 2} \frac{\Delta U}{\Delta P} \quad (S1)$$

where η , κ , ε , L , a , U , P are viscosity of solvent, solvent conductivity, solvent dielectric constant, thickness of pore, radius of pore, streaming potential, and applied pressure, respectively. The value of $\Delta U / \Delta P$ obtained from the slope of linear fit in Fig. S2(B) yields $\zeta = -5.01 \pm 0.25$ mV. When the electrical potential (ψ) $\ll \frac{2k_B T}{e}$, the surface charge (σ) is;

$$\sigma = \frac{\varepsilon \zeta}{\lambda} \quad (S2)$$

where λ is Debye length, which is calculated by $\lambda = \sqrt{\frac{\varepsilon k_B T}{2e^2 n_0}}$. Using ζ -potential value, the surface charge of silicon nitride is -7.24 ± 0.36 mC/m². A more rigorous extraction of zeta potential in the limit of dU/dP as $P \rightarrow 0$ uses a quadratic fit of the data (black solid curve Fig S2B) and yields $\zeta = -3.22 \pm 0.26$ mV and a silicon nitride surface charge of -4.65 ± 0.38 mC/m². Thus, it should be noted that different protocols for fitting data such as that shown in Fig. S2(B) can lead to variations in the surface charge. However, given the ultrathin nanopore shape and the fact that

transport is an electrokinetic phenomenon having both electrophoretic and electroosmotic components, the value of this surface charge has little effect on the overall force applied to the translocating protein. In the cases considered here, the experimental surface charge had no effect on the MD simulations because of the large driving forces that were applied. When setting up the MD simulations, we did not attempt to match the experimental surface charge of the nanopores because of the high effective biases that were applied in the simulations. Combined with the high molarity of the electrolyte, the effect of the surface charge is therefore considered to be negligible.

4. Open pore conductance for different pore diameters

Table S1: Conductance values for different pore diameters: The conductance values were obtained using Ohm's law for an electrolyte in a cylinder and from the slope of current vs voltage data (see Fig. S21 in Sec. 20) and were used to estimate the effective pore length L as described in previous reports (1, 2, 7). Error values in the conductance represents the errors obtained in the slopes of the current vs voltage data when fitted with a straight line (Fig. S21). The nanopores were fabricated and their diameters measured using transmission electron microscopy (TEM).

Pore Diameter (nm)	Conductance (nS)	Pore Length (nm)
5.5	23.02 ± 0.07	7.1
3.5	12.55 ± 0.02	6.0
3	11.78 ± 0.05	4.3
2.5	10.08 ± 0.02	3.4
2	6.13 ± 0.04	4.1
1.5	5.28 ± 0.04	2.5

5. Electric field and dipole orientations

If the minimization of the potential energy ($-p \cdot E$) due to alignment of the electric dipole (p) of cyt c along the electric field (E) is greater than the thermal energy ($\frac{3}{2} k_B T$), then cyt c would begin to trap in an orientation along the electric field. For $p \cdot E > \frac{3}{2} k_B T$, the requirement is $E > 1.5 k_B T / p$. Putting in literature values (8) of $p = 320 \times 0.0208$ e-nm and $k_B T = 25.7$ meV, suggests that in an electric field $E > 5.8$ MV/m, cyt c will begin to orient itself along the electric field. Assuming linear drops of electric potential inside the pore from the trans to the cis direction and thus a constant electric field inside the pore, our experimental electric fields are ~ 8 -30 times larger than the threshold electric field 5.8 MV/m. Even though there will be some attenuation of the field strength at the mouth of the pore, the fields used here are sufficient to induce a strong dipolar orientation of the protein molecule at the mouth of the pore before its translocation.

6. Representative current traces for cyt c using a 2.5 nm pore at different voltages

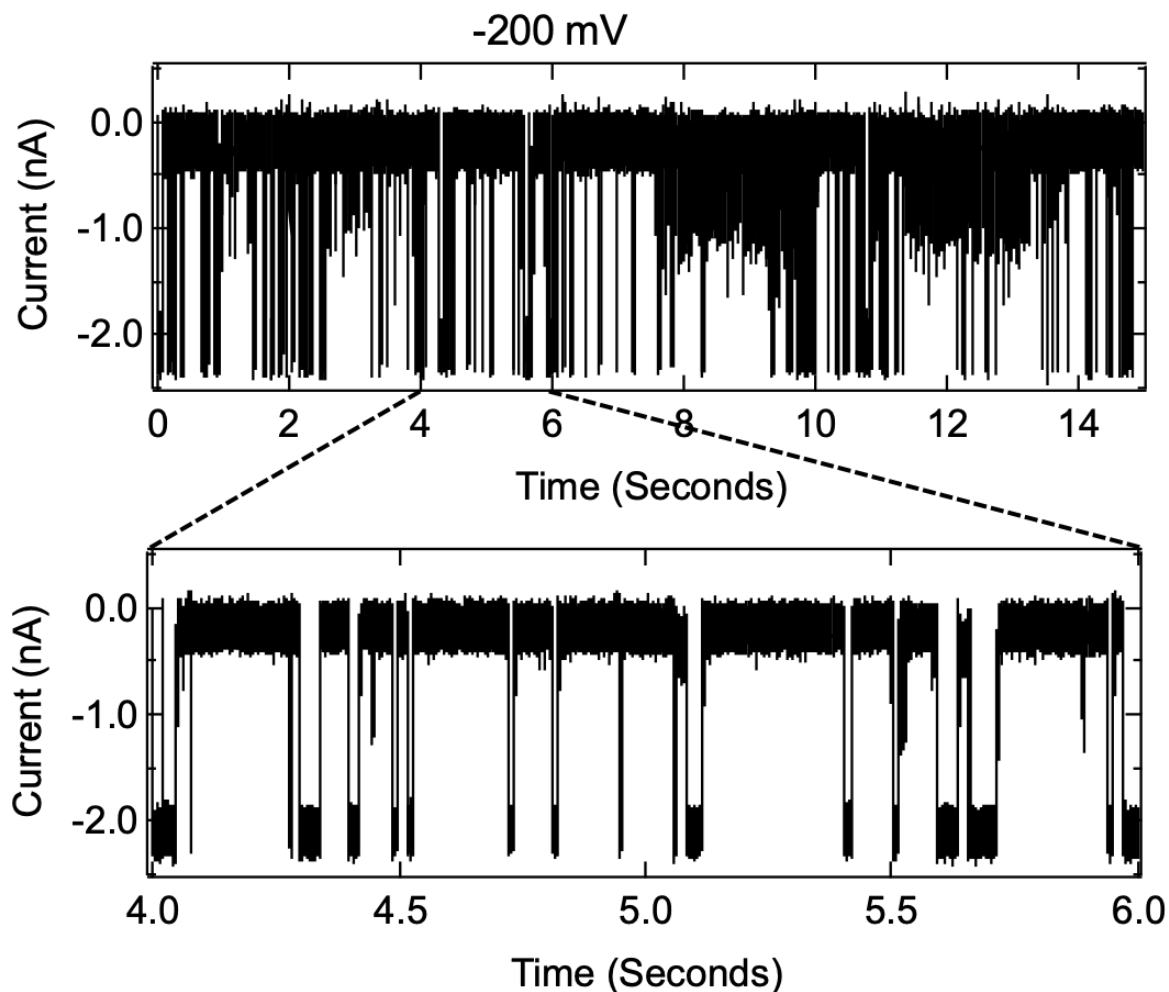


Figure S3(i) Ionic current traces for cyt c using a 2.5 nm pore at -200 mV applied voltage. The measurements were carried out in 1M, KCl, 10mM HEPES, pH 7.5, sampling rate of 250 kHz, and filtered using a low-pass Bessel filter of 100 kHz. Open pore current value is $\cong -2$ nA.

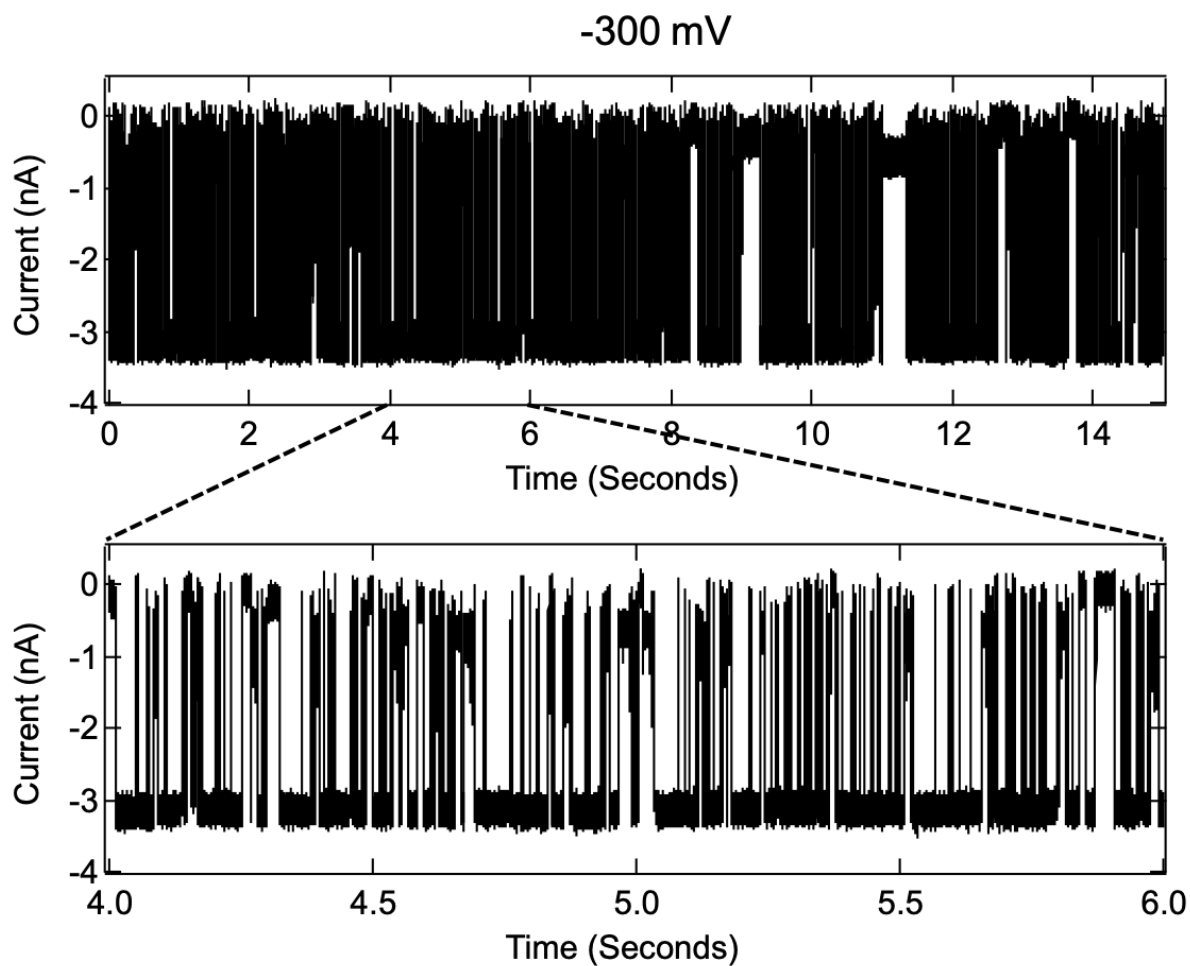


Figure S3(ii) Ionic current traces for cyt c using a 2.5 nm pore at -300 mV applied voltage. The measurements were carried out in 1M, KCl, 10mM HEPES, pH 7.5, sampling rate of 250 kHz, and filtered using a low-pass Bessel filter of 100 kHz.

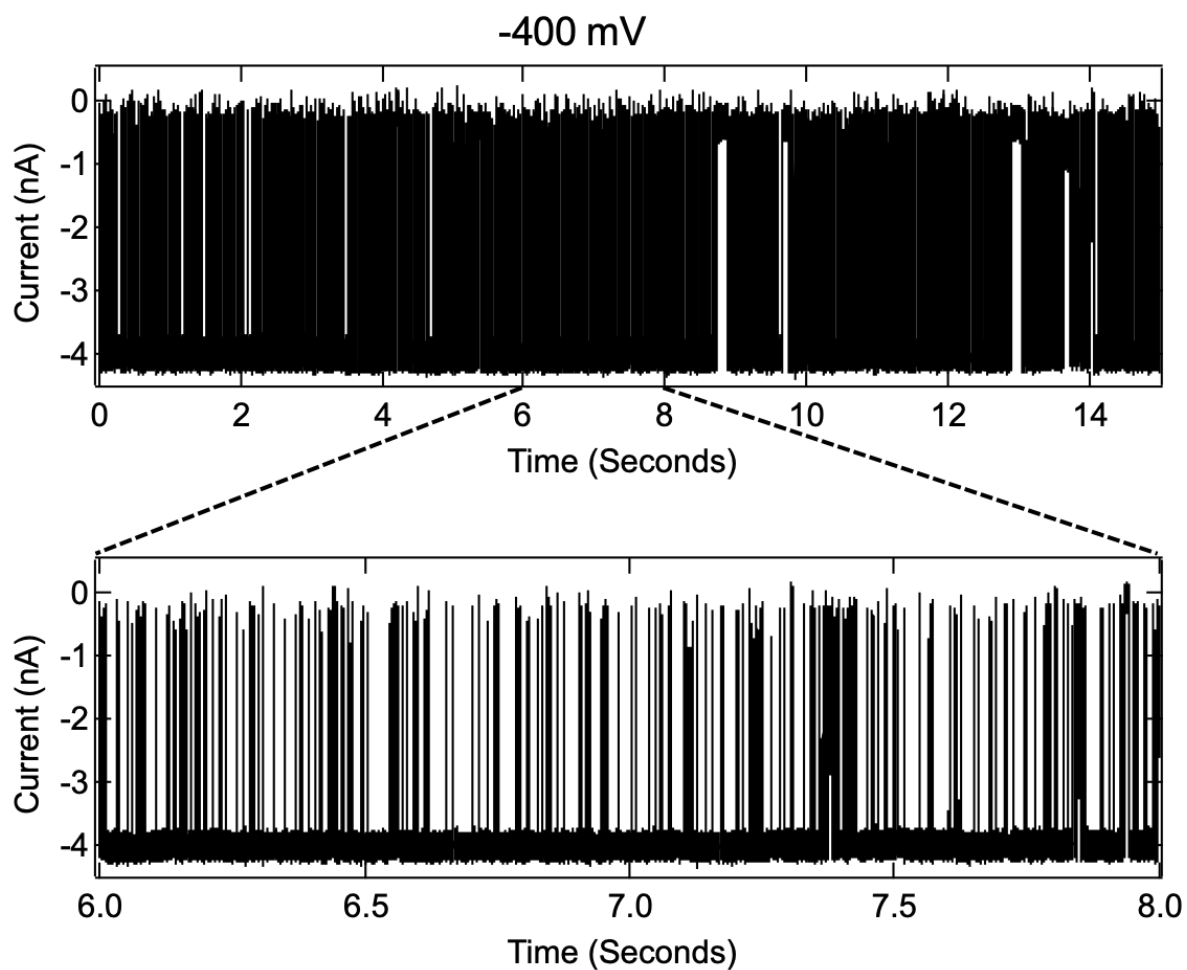


Figure S3(iii) Ionic current traces for cyt c using a 2.5 nm pore at -400 mV applied voltage. The measurements were carried out in 1M, KCl, 10mM HEPES, pH 7.5, sampling rate of 250 kHz, and filtered using a low-pass Bessel filter of 100 kHz.

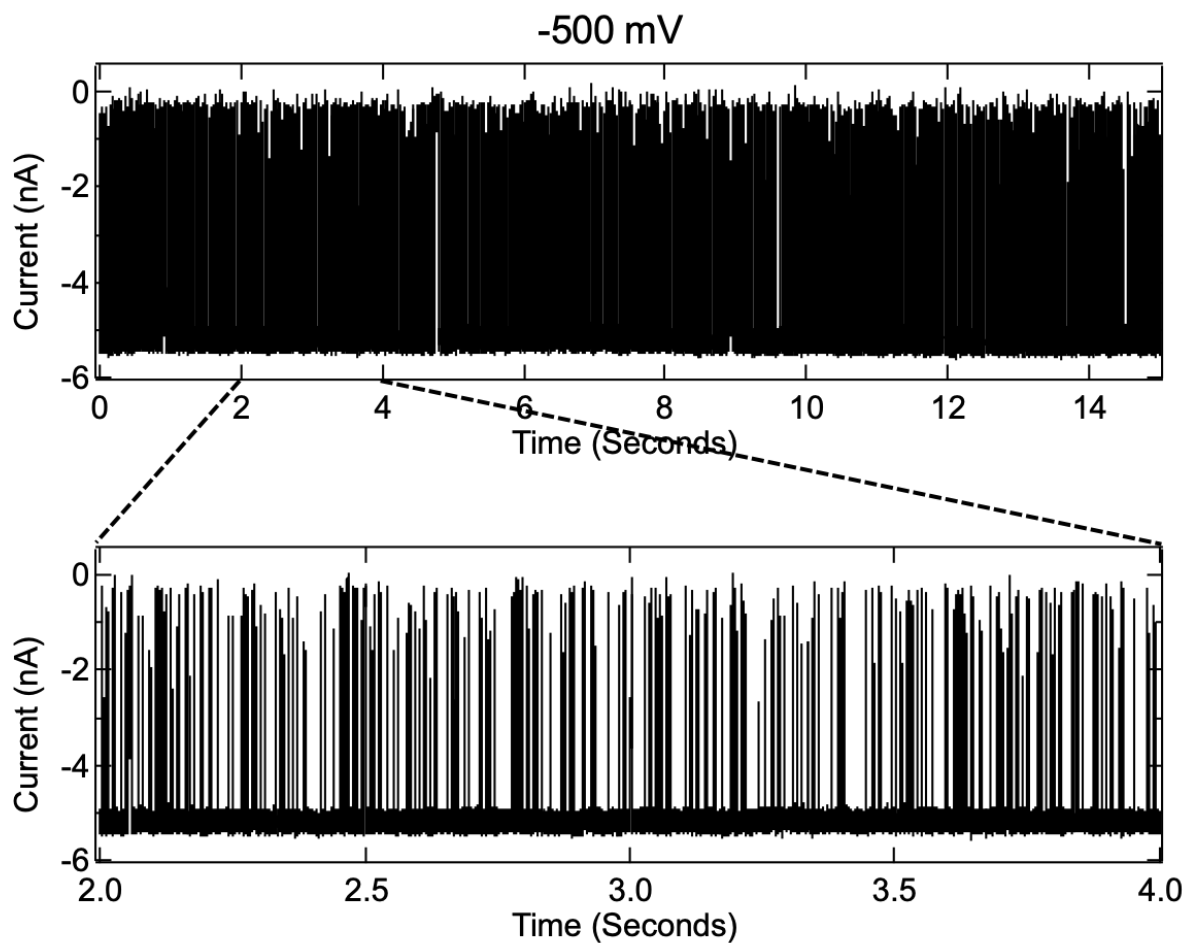


Figure S3(iv) Ionic current traces for cyt c using a 2.5 nm pore at -500 mV applied voltage. The measurements were carried out in 1M, KCl, 10mM HEPES, pH 7.5, sampling rate of 250 kHz, and filtered using a low-pass Bessel filter of 100 kHz.

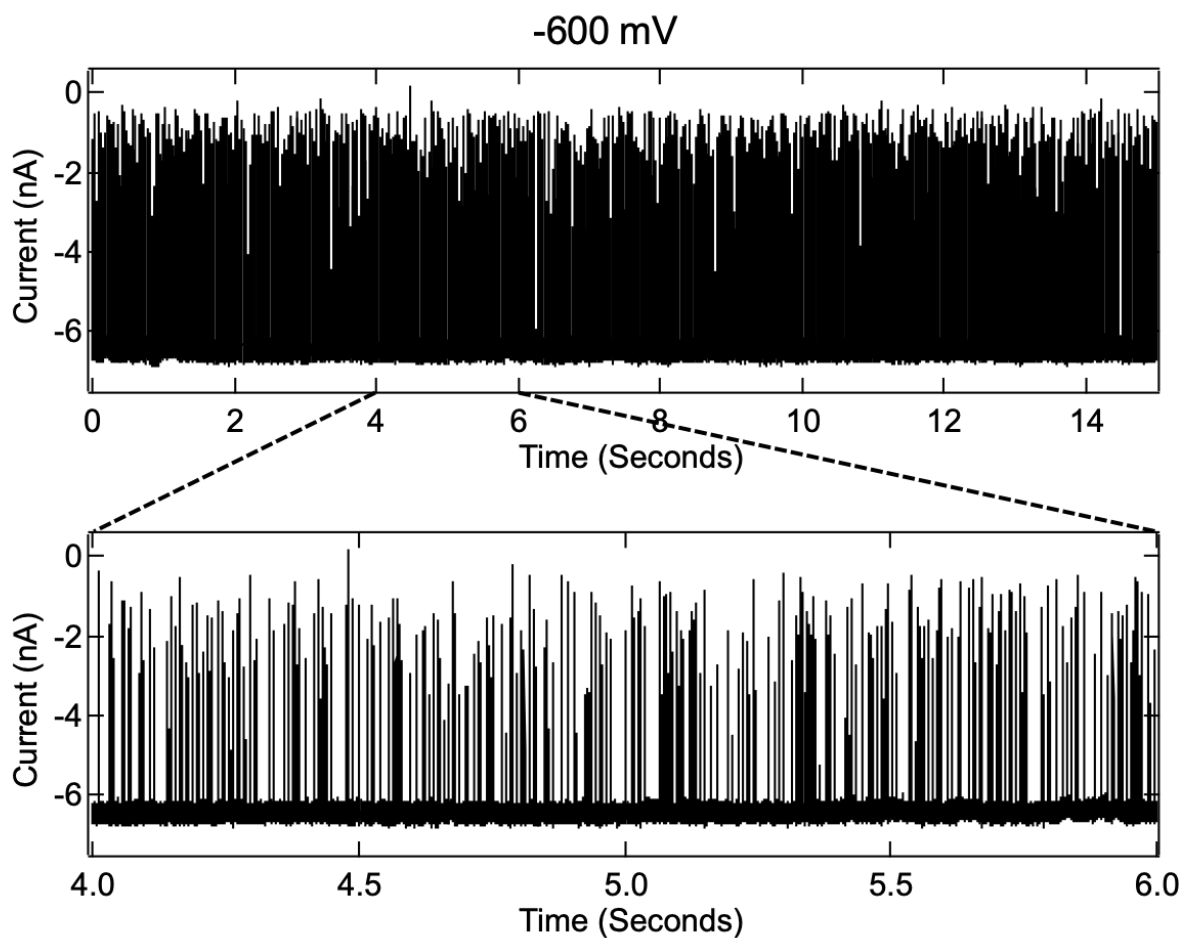


Figure S3(v) Ionic current traces for cyt c using a 2.5 nm pore at -600 mV applied voltage. The measurements were carried out in 1M, KCl, 10mM HEPES, pH 7.5, sampling rate of 250 kHz, and filtered using a low-pass Bessel filter of 100 kHz.

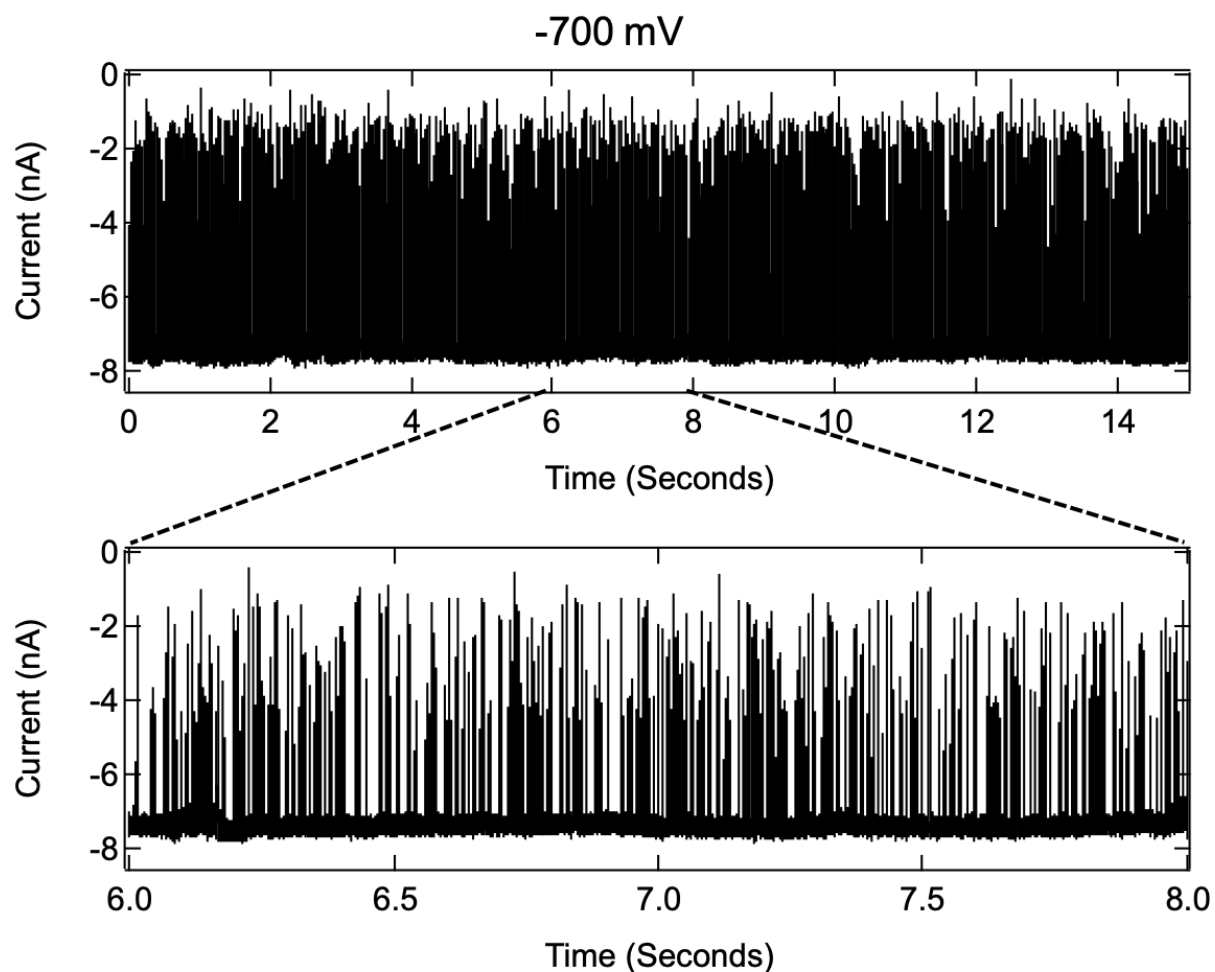


Figure S3(vi) Ionic current traces for cyt c using a 2.5 nm pore at -700 mV applied voltage. The measurements were carried out in 1M, KCl, 10mM HEPES, pH 7.5, sampling rate of 250 kHz, and filtered using a low-pass Bessel filter of 100 kHz.

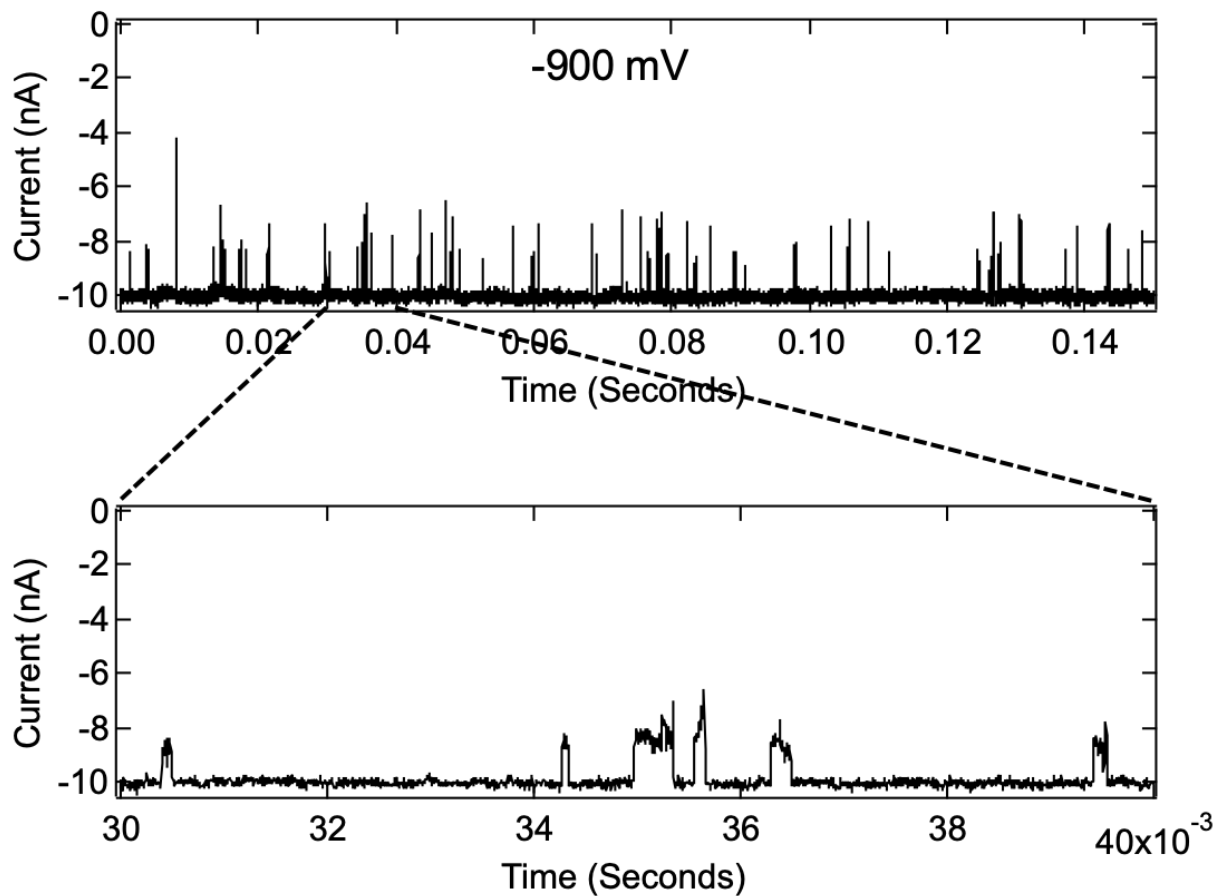


Figure S3(vii) Ionic current traces for cyt c using a 2.5 nm pore at -900 mV applied voltage. The measurements were carried out in 1M, KCl, 10mM HEPES, pH 7.5, sampling rate of 250 kHz, and filtered using a low-pass Bessel filter of 100 kHz.

7. Two-state model for $\Delta I/I_o$ vs. E_{app} in the dynamical unfolding limit (for 2nm pore)

An example of the two-state model for a field-dependent fractional blockade is given by Eq. 2 in the text:

$$\left\langle \frac{\Delta I}{I_o} \right\rangle_{MI} = \mathcal{N}^{-1} \left[\phi_M e^{\frac{\Delta\Delta G_{MI} + \Delta\Delta H_{MI}^{E_{app}}}{k_B T_0}} + \phi_I \right] \quad (S3)$$

where $\mathcal{N} = e^{\frac{\Delta\Delta G_{MI} + \Delta\Delta H_{MI}^{E_{app}}}{k_B T_0}} + 1$. Boltzmann's constant is denoted by k_B and T_0 is room temperature. This equation was applied to analyze the interconversion of two conformational states on the unfolding pathway (M and I, where $G_M < G_I$ in zero applied field). A single cyt c molecule is suggested to be trapped and retained by an electric field at the mouth of the 2.0 nm pore, giving rise to the level i blockade changes as the electric field is increased. The fractional blockades for the I-state and M-state are denoted in Eq. S3 by ϕ_I and ϕ_M , respectively. The energies and the difference dipoles are referenced to the native state so that: $\Delta\Delta G_{MI} = \Delta G_{NI} - \Delta G_{NM}$. For the limit where the permanent dipole term in Eq. 1 of the text is dominant, we have:

$$\Delta\Delta H_{MI}^{E_{app}} = \Delta p_{NM} E_{app} - \Delta p_{NI} E_{app} = (p_M - p_N - (p_I - p_N)) E_{app} = -\Delta p_{MI} E_{app}. \quad (S4)$$

For the limit where the induced dipole term in Eq. 1 of the text is dominant, we have:

$$\Delta\Delta H_{MI}^{E_{app}} = \Delta\alpha_{NM} E_{app}^2 - \Delta\alpha_{NI} E_{app}^2 = (\alpha_M - \alpha_N - (\alpha_I - \alpha_N)) E_{app}^2 = -\Delta\alpha_{MI} E_{app}^2. \quad (S5)$$

Thus, as the field increases, the more energetic I-state is lowered relative to the M-state and their respective fractional blockades at the mouth of the 2.0 nm pore can be found by fitting the level i blockade data shown in Fig. 2C of the main text. It should be emphasized that the fractional blockade for a given state is strongly dependent upon both the pore size and whether or not the given conformation is interconverting at the mouth of the pore or is trapped (i.e., squeezed) more deeply inside the pore.

8. Representative current traces for cyt c using different pore diameters at -100 mV

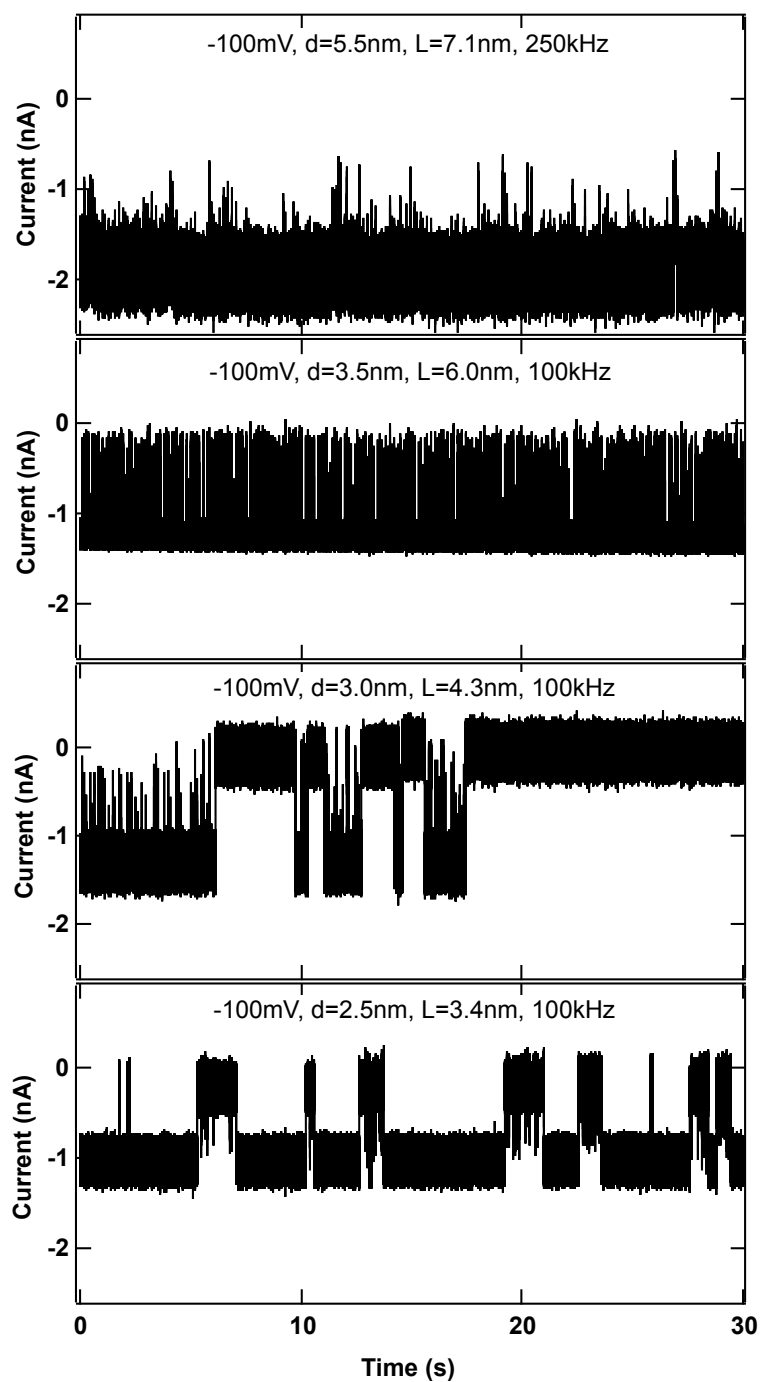


Figure S4 Ionic current traces for cyt c using pores in the diameter range of $2.5 \text{ nm} < d_{\text{pore}} < 5.5 \text{ nm}$ at -100 mV applied voltage. The measurements were carried out in 1M, KCl, 10mM HEPES, pH 7.5. The 5.5 nm pore data was measured using Chimera VC100 Instruments, and filtered at low pass Bessel filter of 250 kHz whereas all other data were measured using Axopatch and filtered at 100 kHz.

9. Representative current traces for cyt c using 2.0 nm and 1.5 nm diameter pores.

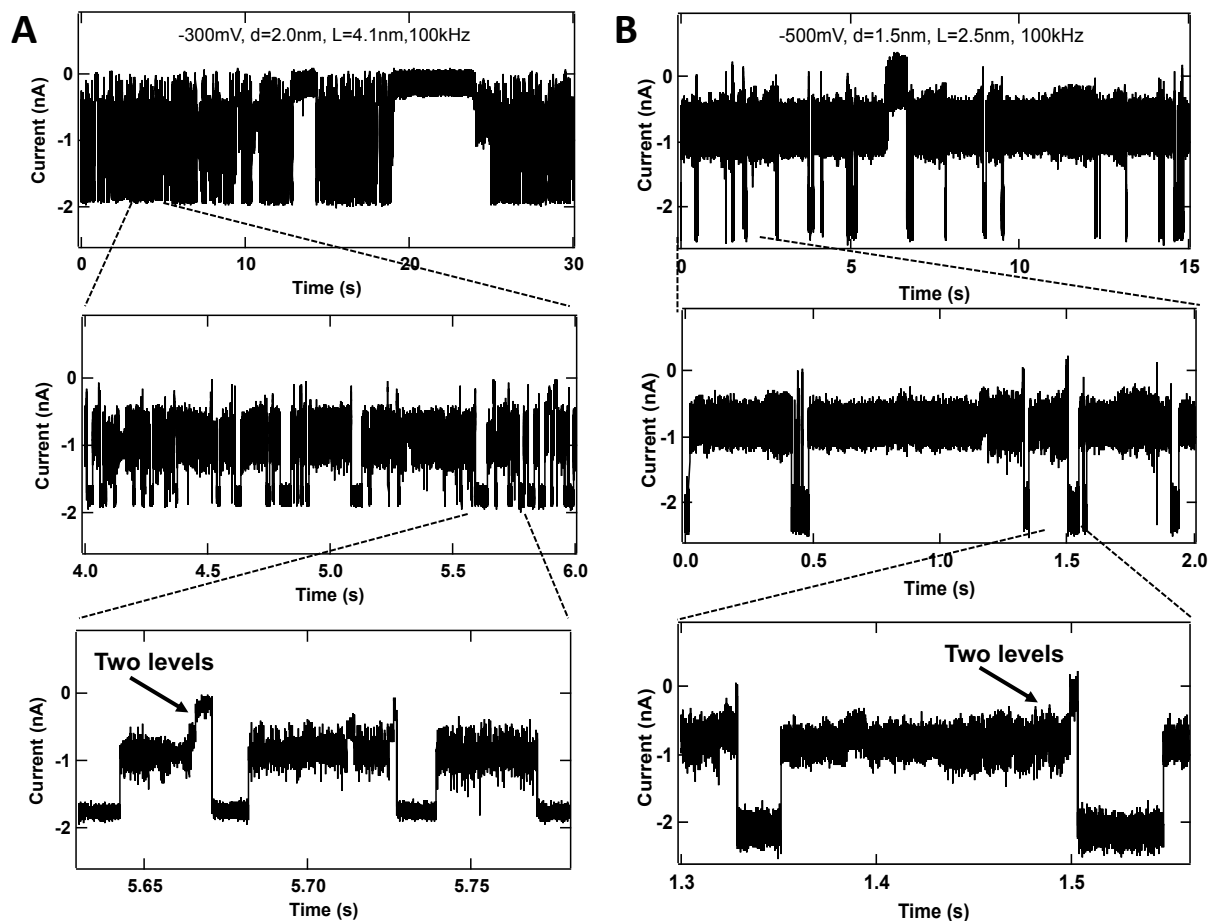


Figure S5 Ionic current traces for cyt c using **(A)** a 2.0 nm diameter pore at -300 mV, and **(B)** a 1.5 nm diameter pore at -500 mV. The measurements were carried out in 1M, KCl, 10mM HEPES, pH 7.5. The data were filtered at 100 kHz and recorded at a sampling rate of 250 kHz. Two-level events were rarely observed below a threshold voltage strength -250 mV for the 2nm pore and -500 mV for the 1.5 nm pore.

10. Representative $\Delta I/I_o$ histograms and fraction of events with level ii for cyt c using a 2.0 nm pore.

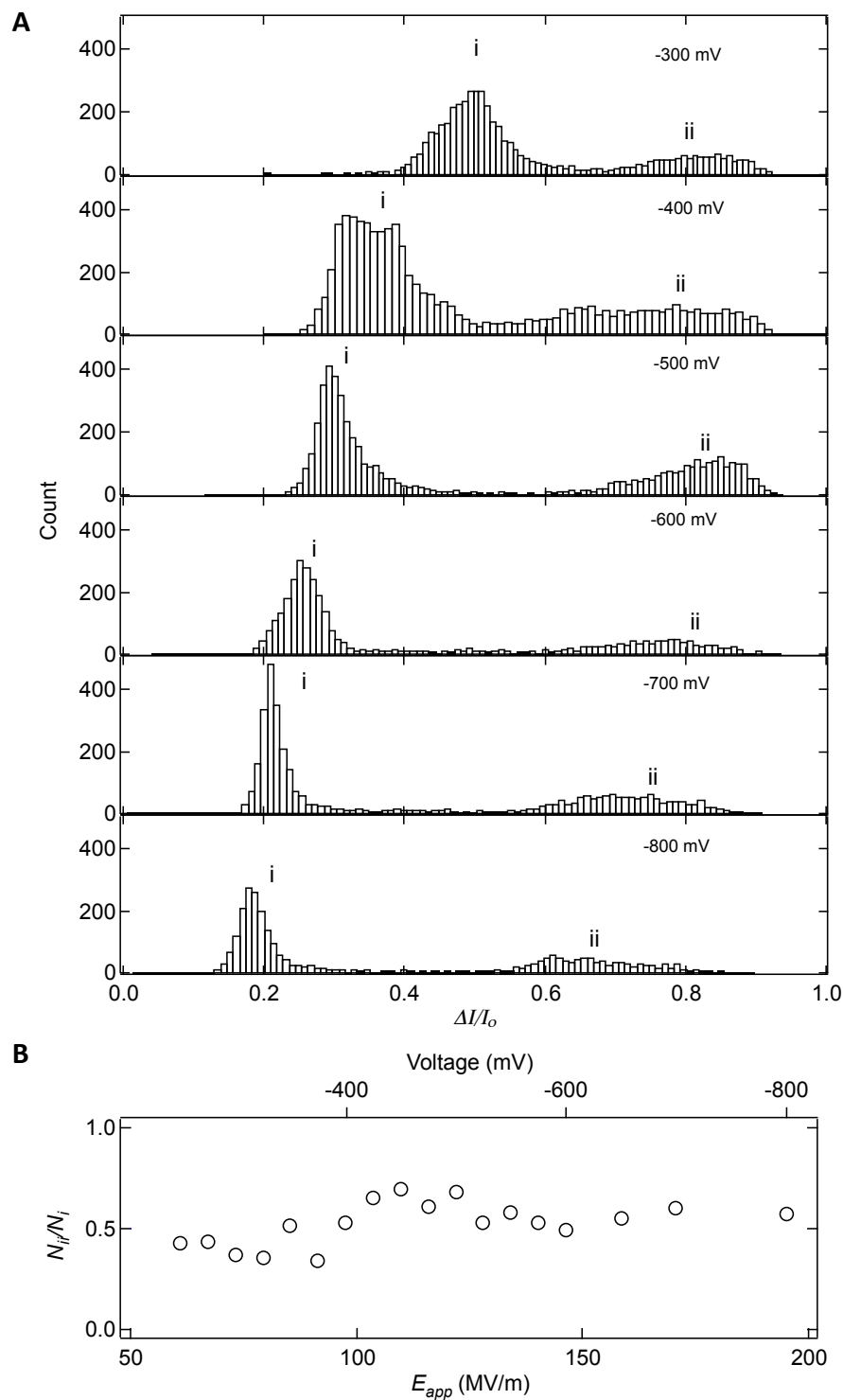


Figure S6. (A) Representative histograms of $\Delta I/I_o$ measured for a 2nm pore ($L = 4.1$ nm) at various voltages and (B) fraction of level ii events. The histograms show two clear populations (level i and level ii) with the peak position of level i decreasing with voltage.

11. MD simulation methods and data for 1.5 nm pore.

i: Molecular models and general systems preparation

The hexagonal patches of Si₃N₄ membranes were generated using the Inorganic Builder plugin of VMD (9). The membranes were aligned with the x-y plane of the coordinate system. By the removal of atoms from the membrane, a double-cone pore was created in each membrane. The axis of the cone was aligned with the z-axis. The minimum diameter of the cone was set to be at the middle of the membrane (which henceforth is called pore diameter); the cone angle was 15° degrees (with respect to the z axis). The charge of the atoms comprising the Si₃N₄ membrane was adjusted by a small (< 0.1%) amount to make the Si₃N₄ membrane neutral. Table S2 summarizes the geometry of the simulated systems. Initial atomic coordinates of cytochrome c were taken from the crystal structure reported by Bushnell et al (PDB code: 1HRC) (10). Missing hydrogen atoms were added to the protein using the PSFGen plugin of VMD. The minimum distance between the protein and membrane was set to be at least 15Å away from the membrane surface to ensure that, at the beginning of the simulation, there were no contact forces between the membrane and the protein. Next, a pre-equilibrated volume of TIP3 water was added to the system using the Solvate Plugin of VMD (11). Following that, potassium and chloride ions were added using the Autoionize VMD plugin to produce 1 M KCl solution.

Table S2: Geometry of the simulated systems

Pore diameter (nm)	Membrane thickness (nm)	Simulation box size* (nm × nm)	Number of atoms	
			Open pore	Protein + pore
1.5	2.5	3.8 × 11.4	53619	53148
2.0	4.1	3.8 × 13.2	61669	61129
2.5	3.4	3.8 × 12.3	57664	57124
3.0	4.3	3.8 × 13.4	63061	62484
3.5	6.0	4.2 × 14.9	85037	84457
5.5	7.1	5.7 × 16.1	169241	168741

*The box size is specified as the side edge length of the hexagonal prism and the height of the simulation box.

ii: Molecular dynamics simulation

All of the simulations were performed using the molecular dynamics program NAMD2 (12). To describe the atomic interactions in the simulations, CHARMM36 (13) force field parameters for the protein and ions, TIP3P model for water and the custom force field describing crystalline Si₃N₄ (14) were used. For van der Waals and short-range electrostatic interactions, a smooth cutoff of 12 Å with a switching function starting at 10 Å was used. Long range electrostatic interactions were evaluated with particle mesh Ewald (PME) (15) over a 1 Å-spaced grid. Periodic boundary conditions were employed in all simulations. Each system was minimized using the conjugate

gradient method for 5000 steps followed by an NPT equilibration run of 10 ns at 295 K and 1 atm. The constant pressure was realized using a Nose-Hoover Langevin piston (16) and temperature was maintained at a constant value by coupling the system to a Langevin thermostat (17).

iii: Simulation Protocols

To simulate electric field-driven transport of cyt c through the Si₃N₄ nanopores, grid-steered molecular dynamics (G-SMD) method (18) was employed. In this method, nanopore transport of biomolecules is accelerated by subjecting the solute's atoms to a grid-based potential that accurately reproduces the distribution of the electrostatic potential in the nanopore system. The accelerated transport of the solute is obtained when the force from such a grid-based potential is amplified along the direction of the nanopore transport and selectively applied to the atoms of the solute. In our case, the distribution of the electrostatic potential was determined by simulating each nanopore system for 10 ns in pure 1M KCl solution (without the cyt c protein) under a 1V transmembrane voltage. The voltage V was generated by applying a constant electric field $E = -V/L_z$ along the z axis, where L_z is the length of the simulated system along the direction of the applied electric field (19). As the resulting distribution of the electrostatic potential was highly non-homogeneous (especially within the pore) and depended on the pore geometry, the open pore simulations were performed for each pore geometry. The average distributions of the electrostatic potential was then calculated and averaged over the respective MD trajectory using the PMEpot Plugin of VMD (19), producing a 1 Å-spaced grid potential. In the G-SMD simulations of the nanopore transport, the potential was applied to all atoms of the cyt c protein with the scaling factor of 1, 2 or 3 for the z component of the electric field and 0 for the x and y components. The force applies to each atom of the cyt c molecule by the external grid potential was scaled by the partial charge of that atom. In addition to G-SMD, a custom colvar script was used to harmonically restrain the protein's center of mass to the nanopore axis; the spring constant was 10 kcal/(mol Å²). The effect of the small surface charge on the thin silicon nitride membrane was considered negligible in these calculations because of the large bias voltages and the high molarity of the electrolyte that are employed.

iv. Analysis of the simulation results

VMD was used to analyze and post process the simulation trajectories. The steric exclusion model (SEM) (20) of nanopore conductance was used to measure the fractional blockade current during the protein permeation. As aforementioned in the previous section, the membrane (as well as the simulation box) was a hexagonal prism, however, the SEM is developed for a cubic simulation box. Therefore, SEM was only applied to the largest inscribed rectangular in the hexagon of the membrane (See Fig. S7). To quantify the deformation/unfolding state of the protein during the permeation, the fraction of native contacts, Q-value (21), was calculated for the structured parts (sheets and helices) of the protein in each simulation. For calculating the Q-value, the reference structure of the protein was the initial crystal structure of the protein.

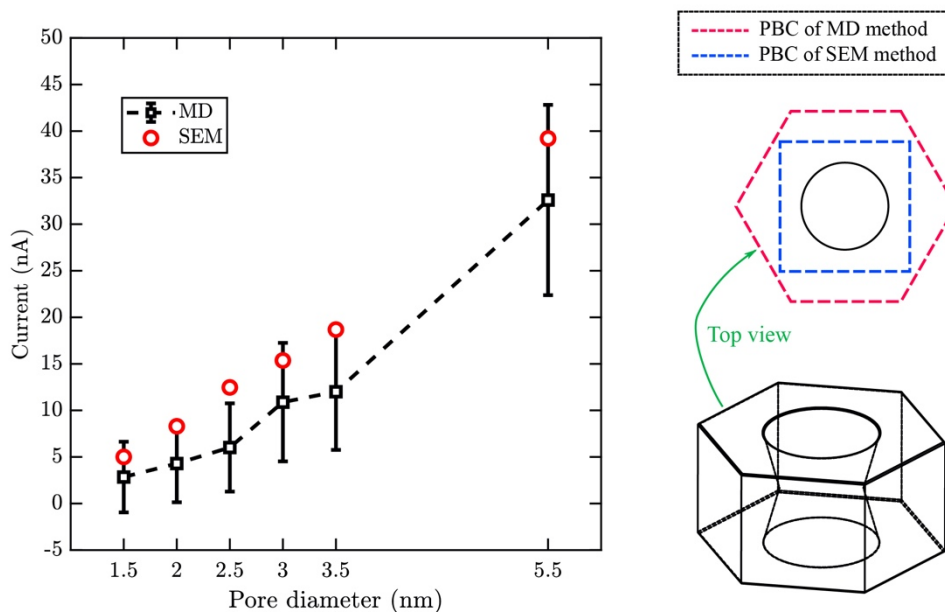


Figure S7. Open-pore currents obtained directly from all-atom simulations (black) and from SEM calculations (red). Each MD current value was obtained by averaging instantaneous ion displacements over a 10 ns MD trajectory at 1V bias. The error bars show the standard deviations of the 5 ps-sampled current traces; the dashed line is the guide to the eye. The bottom right image shows a schematic 3D representation of the simulated Si_3N_4 membrane whereas the top right image shows how the system's cross section is represented in SEM.

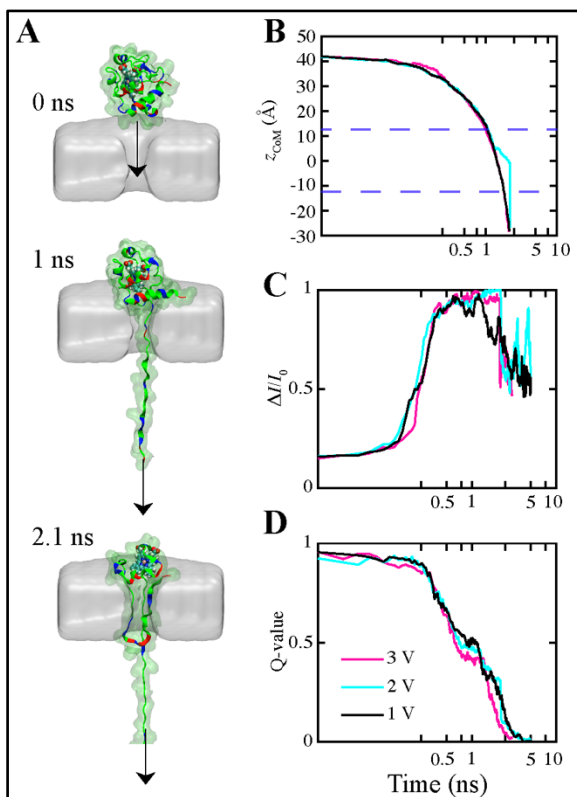


Figure S8. MD simulation of cyt c translocation through a 1.5 nm pore. **(A)** Snapshots representing an MD trajectory where a single cyt c protein was forced to pass through a 1.5 nm nanopore (gray) using the G-SMD protocol under a 3V effective bias and the constant velocity SMD pulling (illustrated by the black arrow). **(B-D)** CoM z coordinate (B), ionic current blockade (C) and cyt c Q-value (D) versus simulation time for three simulations carried out at the specified effective biases. In addition to G-SMD, the N-terminus of the protein was pulled along the nanopore axis with 0.1 Å/ps velocity using the SMD protocol; the SMD spring constant was 5.5 kcal/(mol Å²). The SEM approach was used to calculate the ionic current blockades. Note the logarithmic scale of the horizontal axis.

12. Distributions of $\Delta I/I_o$ as a function of voltage for cyt c using a 3.0 nm pore.

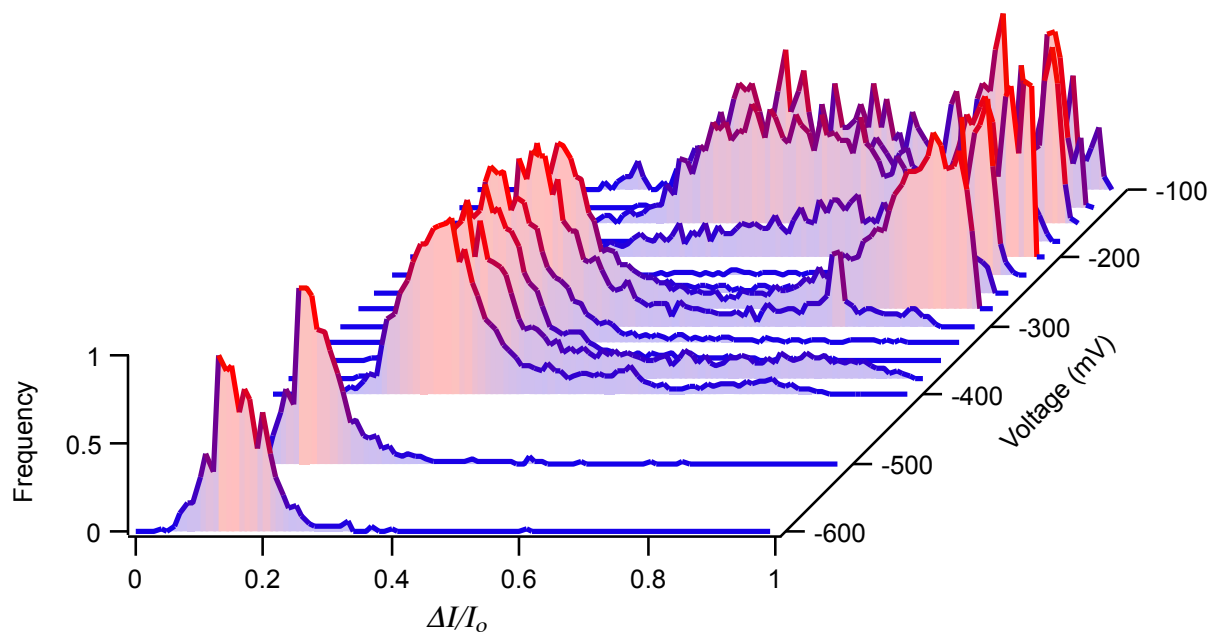


Figure S9. Distributions of fractional change in current as a function of applied voltage measured for cyt c using a 3.0 nm diameter pore, $L = 4.3$ nm (1M KCl, 10mM HEPES, pH7.5).

13. Experiments in presence of Gdm-Cl (Denaturation data)

Table S3: Conductivity of bulk solution and conductance of nanopore ($d_{pore} = 2.5$ nm). The conductance was measured as described in section 3.

Electrolyte solution (10 mM HEPES, pH 7.5)	Conductivity in bulk solution (mS/cm)	Conductance in Nanopore (nS)
0.5M Gdm-Cl, 1M KCl	130 mS/cm	11 nS
1M Gdm-Cl, 1M KCl	158 mS/cm	13 nS
2M Gdm-Cl, 1M KCl	207 mS/cm	14.5 nS
3M Gdm-Cl, 1M KCl	240 mS/cm	16.6 nS

Figure S10. Ionic current traces for cyt c ($0.5 \mu\text{M}$) translocation in 2M Gdm-Cl, 1M KCl, 10mM HEPES, pH7.5 solution at different voltages for a 2.5 nm pore ($L=3.4$ nm).

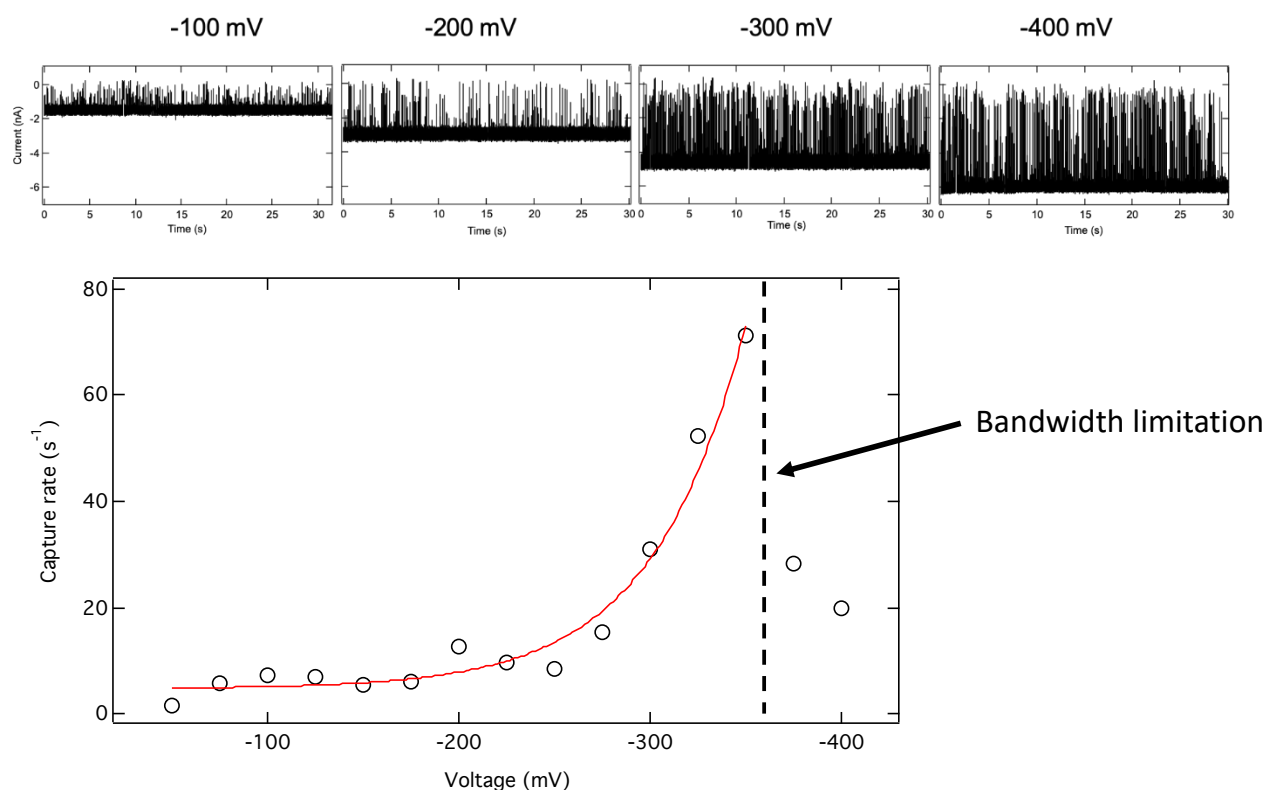


Figure S11. Capture rate as a function voltage for cyt c ($0.5 \mu\text{M}$) using a 2.5 nm pore under 2M Gdm-Cl, 1M KCl, 10mM HEPES, pH 7.5. The red curve represents a fit to the function $y_0 + A e^{-V/V_0}$, with $y_0 = 4.70$, $A = 0.05$, and $V_0 = 48.6$. The observed exponential dependence reflects an entropy barrier for capture, consistent with a blob-like polymer behavior of an unfolded protein. Above -350 mV capture rates were observed to drastically decrease, due to extremely fast translocation pulses for unfolded cyt c, which our limited bandwidth of measurement cannot resolve.

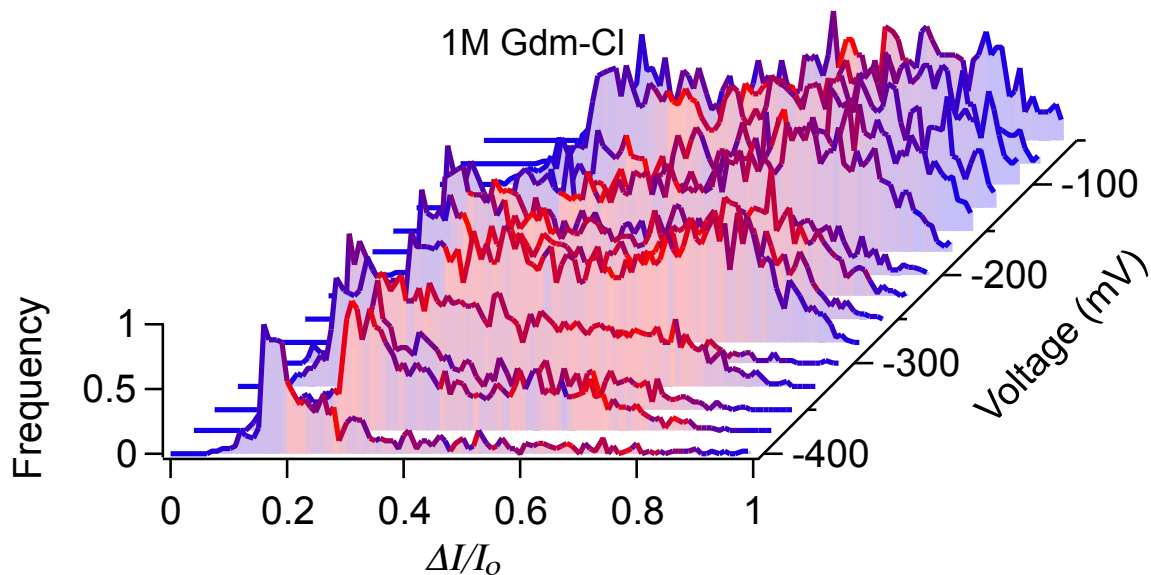


Figure S12. Distributions of fractional blockade as a function of applied voltage measured for cyt c using a 2.5 nm pore. cyt c (0.5 μ M) was incubated in 1 Gdm-Cl, 1M KCl, 10mM HEPES, pH7.5 solution.

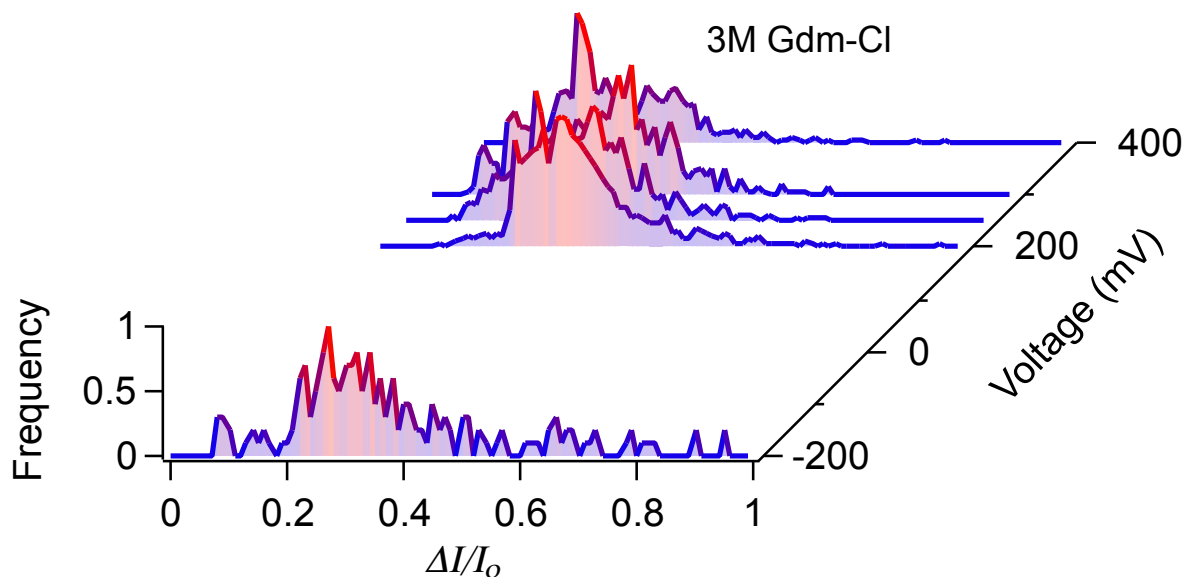


Figure S13. Distributions of fractional change in current as a function of applied voltage measured for a 2.5 nm pore, when 0.5 μ M cyt c were incubated in 3 Gdm-Cl, 1M KCl, 10 mM HEPES, pH7.5 solution.

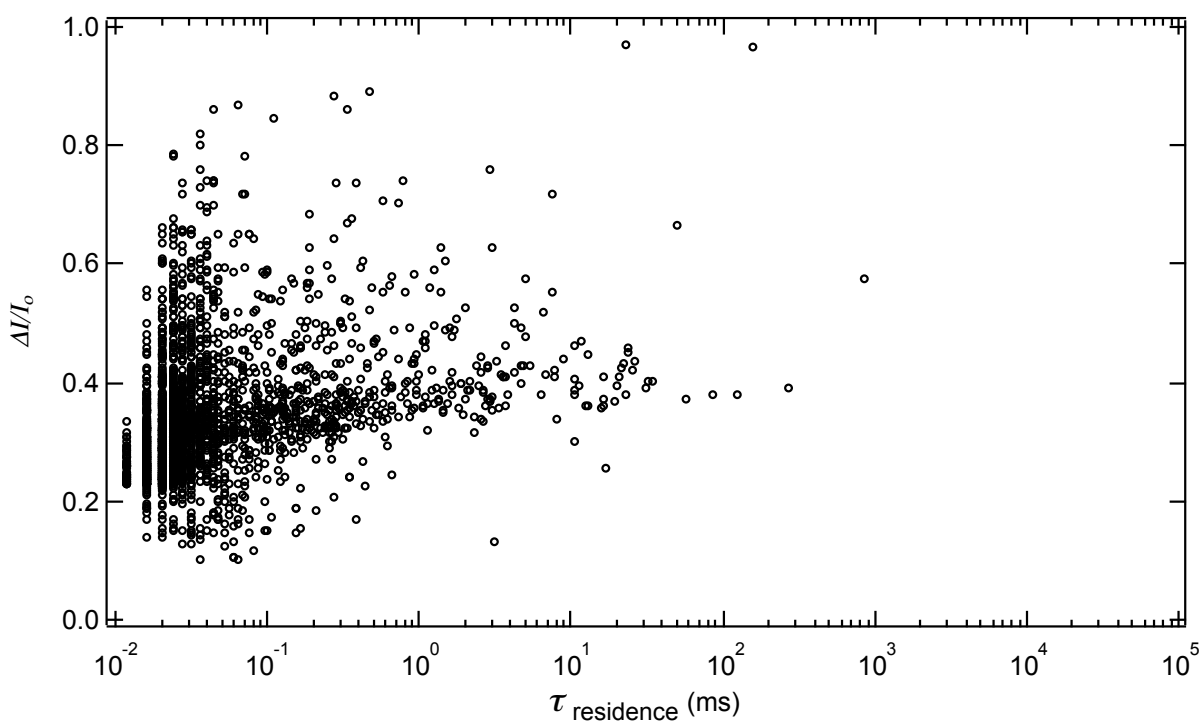


Figure S14. Scatter plots of fractional current blockade and residence time measured at 200 mV and in 3M Gdm-Cl, 1M KCl, 10mM HEPES, pH7.5 solution ($d_{\text{pore}} = 2.5$ nm, $L = 3.4$ nm). The concentration of cyt c used was 0.5 μM .

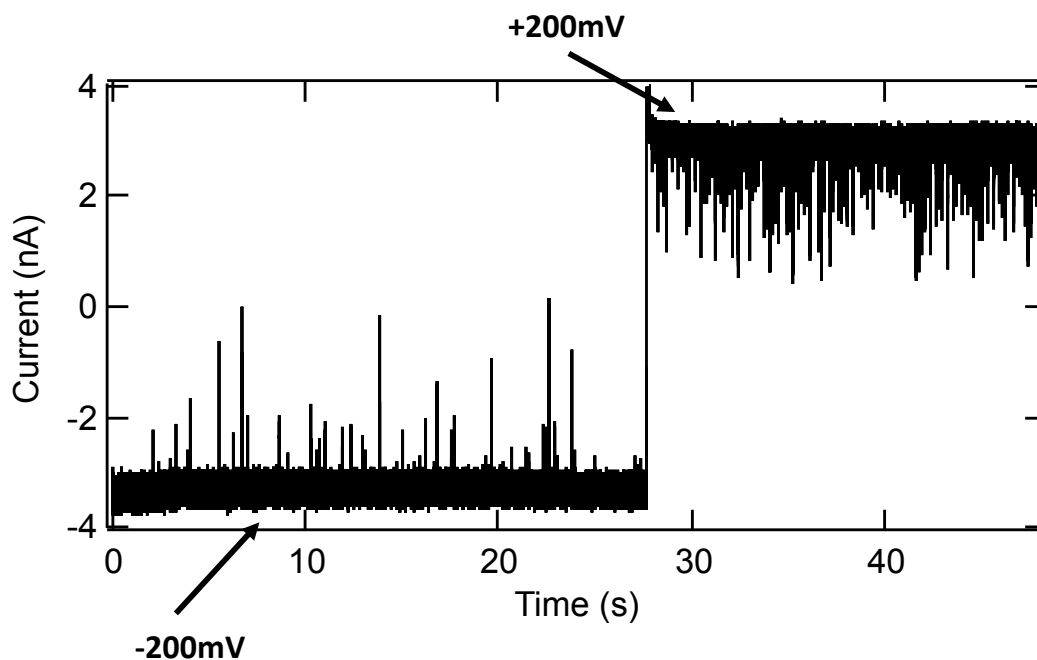


Figure S15. Ionic current trace for cyt c ($0.5 \mu\text{M}$) in 3M Gdm-Cl, 1M KCl, 10mM HEPES, pH7.5 ($d_{\text{pore}} = 2.5 \text{ nm}$, $L = 3.4 \text{ nm}$). We observed translocation events more frequently at +200 mV compared to -200 mV. We did not observe events at positive voltage in other experiments. While we do not understand why this occurs, it could be due to other effects such as charge-reversal of the pore at this high Gdm-Cl concentration, which can influence the mechanism of protein capture at the pore. A similar effect has been observed for poly-ethylene glycol (PEG), where 4 M KCl was used to drive the translocation of the otherwise neutral polymer (22).

14. Multicomponent Gaussian fits to the $\Delta I/I_o$ distributions of cyt c using a 2.5 nm pore

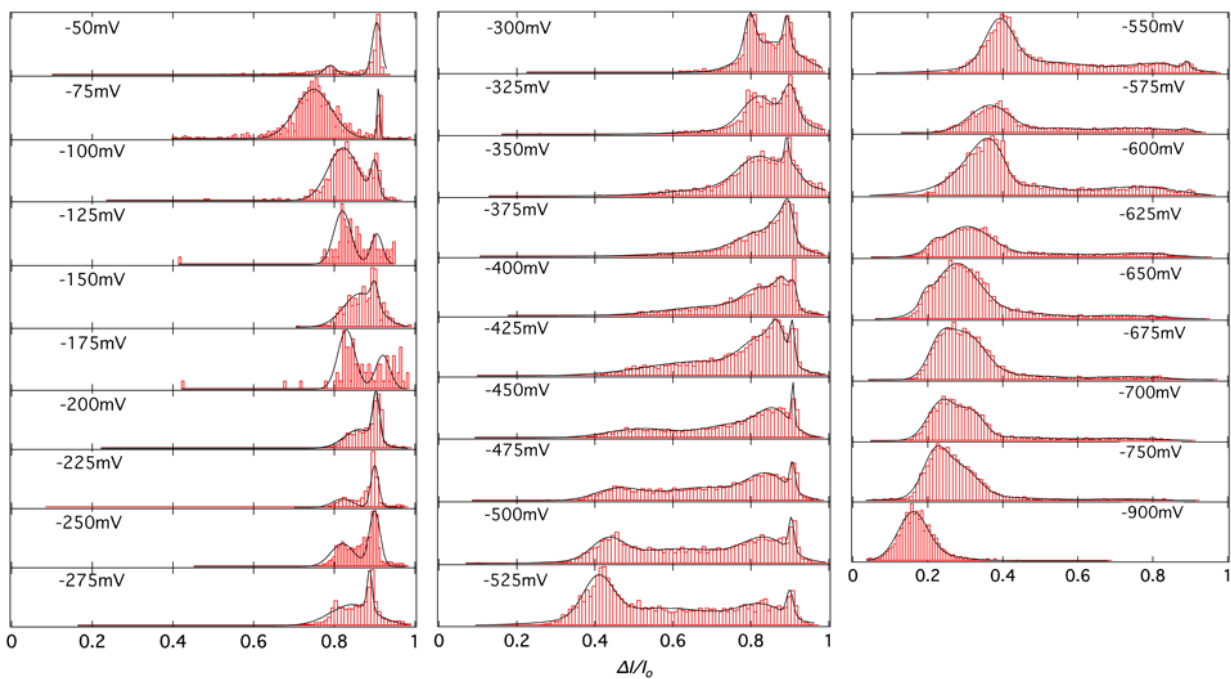


Figure S16. Distributions of $\Delta I/I_o$ and their fits to a multi-component Gaussian function at different voltages for the pore size $d_{\text{pore}} = 2.5\text{nm}$, $L = 3.4\text{nm}$ (1M KCl, 10mM HEPES, pH7.5)

15. Two-state and three-state model for $\Delta I/I_o$ vs. E_{app} in the dynamical unfolding limit (analysis for 2.5 nm pore).

We consider the case where state M squeezes into the 2.5 nm pore under the action of an applied electric field and, as the field is increased, dynamic unfolding and refolding of the three cyt c α -helices can take place. This can be visualized using either a two-state model between M and U or within a three-state scheme where an intermediate I-state, with one of the cyt c α -helices unfolded, is populated. The blockade data for the 2.5 nm pore are shown in Fig. 3E of the text. The sub-states M_1 and M_2 are thought to involve two different, non-interconverting, squeezed pore configurations of cyt c where the stabilizing salt bridge, involving residue E62, has broken and there is a loss of the associated short 2 stranded beta sheet (23). This is followed by Ω -loop unfolding of residues 40-57 and 60-87 (including Met80 dissociation). The two M-states are differently squeezed and configured within the pore and do not appear to interconvert with each other so the configuration notation (1 or 2) can be attached in an *ad hoc* manner.

The 3-state equilibrium average is given by:

$$\left\langle \frac{\Delta I}{I_o} \right\rangle_{MU} = \mathcal{N}^{-1} (\phi_I e^{\frac{\Delta\Delta G_{IU} - \Delta p_{IU} E_{app}}{k_B T_0}} + \phi_M e^{\frac{\Delta\Delta G_{MU} - \Delta p_{MU} E_{app}}{k_B T_0}} + \phi_U) \quad (S6)$$

with $\mathcal{N} = e^{\frac{\Delta\Delta G_{IU} - \Delta p_{IU} E_{app}}{k_B T_0}} + e^{\frac{\Delta\Delta G_{MU} - \Delta p_{MU} E_{app}}{k_B T_0}} + 1$. Where, for simplicity, we have used only the simple permanent dipole difference term as a parameter to describe the action of the electric field on the conformational state free energy. The energy gap parameters can be simplified by using the 2.0 nm pore results for M-I equilibration so that: $\Delta\Delta G_{MU} = \Delta\Delta G_{MI} + \Delta\Delta G_{IU} = 4k_B T_0 + \Delta\Delta G_{IU}$, where the value of $\Delta\Delta G_{MI}$ in Table 1 of the text has been used. Similarly, for a simple oriented dipole with an effective net charge separation (d_i) in each state given by $d_U > d_I > d_M$, we can deduce that: $\Delta p_{MU} = \Delta p_{MI} + \Delta p_{IU} = 44 \text{ Debye} + \Delta p_{IU}$, again using the information from Table 1. This results in a 3-state fitting function for the dynamic transitions in the 2.5 nm pore that can be written as:

$$\left\langle \frac{\Delta I}{I_o} \right\rangle_{MU} = \mathcal{N}^{-1} (\phi_I e^{\frac{(\Delta\Delta G_{MU} - 4k_B T_0) - (\Delta p_{MU} - 44 \text{ Debye}) E_{app}}{k_B T_0}} + \phi_M e^{\frac{\Delta\Delta G_{MU} - \Delta p_{MU} E_{app}}{k_B T_0}} + \phi_U) \quad (S7)$$

with $\mathcal{N} = e^{\frac{(\Delta\Delta G_{MU} - 4k_B T_0) - (\Delta p_{MU} - 44 \text{ Debye}) E_{app}}{k_B T_0}} + e^{\frac{\Delta\Delta G_{MU} - \Delta p_{MU} E_{app}}{k_B T_0}} + 1$. Equation S7 has one additional free parameter compared to a two-state model.

Because the much broader distribution of blockade current ratios for the $M_1 \leftrightarrow U_1$ transition suggests more direct access to the unfolded conformations, we used a 2-state model to fit its blockade ratio in the 2.5 nm pore. In this case, we assume a direct interconversion between M_1 and a broad set of unfolded states U_1 , rather than sequentially passing through the I-state. The two-state model used for the dynamic unfolding was:

$$\left\langle \frac{\Delta I}{I_o} \right\rangle_{MU} = \mathcal{N}^{-1} [\phi_M e^{\frac{\Delta\Delta G_{MU} + \Delta\Delta H_{MU}^{E_{app}}}{k_B T_0}} + \phi_U] \quad (S8)$$

where $\mathcal{N} = e^{\frac{\Delta\Delta G_{\text{MU}} + \Delta\Delta H_{\text{MU}}^{E_{\text{app}}}}{k_B T_0}} + 1$.

We were able to successfully fit the 2.5 nm pore blockage ratio data for both M_1 and M_2 using the two-state model (Eq. S8) as seen in Table S4. Nearly indistinguishable fits were found whether we take $\Delta\Delta H_{\text{MU}}^{E_{\text{app}}} = -\Delta p_{\text{MU}} E_{\text{app}}$ or $-\Delta\alpha_{\text{MU}} E_{\text{app}}^2$. The value of the polarizability difference, $\Delta\alpha_{\text{MU}}$, is presented in Table S4 as an induced dipole ($\Delta\alpha_{\text{MU}} E_{\text{mid}}$), where we used the midpoint fields in Fig. 3E, $E_{\text{mid}} = 140.3$ MV/m and 158.9 MV/m for $M_2 \leftrightarrow U_2$ and $M_1 \leftrightarrow U_1$, respectively.

Table S4: Two-state fitting (4 free parameters) for the experimental data ($d_{\text{pore}} = 2.5$ nm, $L = 3.4$ nm) in Fig. 3E using Eq. S8 with either Δp_{MU} or $\Delta\alpha_{\text{MU}}$ set to zero.

Parameters	$M_1 \leftrightarrow U_1$	$M_2 \leftrightarrow U_2$
ϕ_M	0.91	0.82
ϕ_U	0.24	0.20
$\Delta\Delta G_{\text{MU}}$	$8.9 k_B T_0$ (5.3 kcal/mol)	$8.2 k_B T_0$ (4.9 kcal/mol)
Δp_{MU}	70.2 Debye	71 Debye
$\Delta\alpha_{\text{MU}} E_{\text{mid}}$	73 Debye	81.5 Debye

We also fit the data with the 3-state model, Eq. S7, which assumes that intermediate I between M and U is also accessed. In order for the fits to converge, we found that the blockade ratio for the I-state must be similar to that of the M-state, consistent with unfolding of only one of the three α -helices. In this scenario for the 2.5 nm pore, both M and I lead to high blockade ratios because they still contain significant α -helical content that evidently leads to ion current blockage. The fitting results for the dynamics of the 3-state system are given in Table S5, where we have constrained ϕ_I by using $\phi_I = \phi_M$ so that only 4 free parameters are needed for the fit.

Table S5: 3-state fitting (4 free parameters) for the experimental data ($d_{\text{pore}} = 2.5$ nm, $L = 3.4$ nm) in Fig. 3E using Eq. S7.

Parameters	$M_1 \leftrightarrow I \leftrightarrow U_1$	$M_2 \leftrightarrow I \leftrightarrow U_2$
ϕ_M	0.91	0.86
ϕ_I	0.91	0.86
ϕ_U	0.23	0.18
$\Delta\Delta G_{\text{MI}}$	$4.0 k_B T_0$ (2.4 kcal/mol)	$4.0 k_B T_0$ (2.4 kcal/mol)
$\Delta\Delta G_{\text{MU}}$	$11.2 k_B T_0$ (6.6 kcal/mol)	$9.1 k_B T_0$ (5.4 kcal/mol)
Δp_{MI}	44 Debye	44 Debye
Δp_{MU}	101.5 Debye	91.4 Debye

16. Representative histograms of $\tau_{\text{residence}}$ for a 2.5 nm pore ($L = 3.4$ nm) at higher electric fields

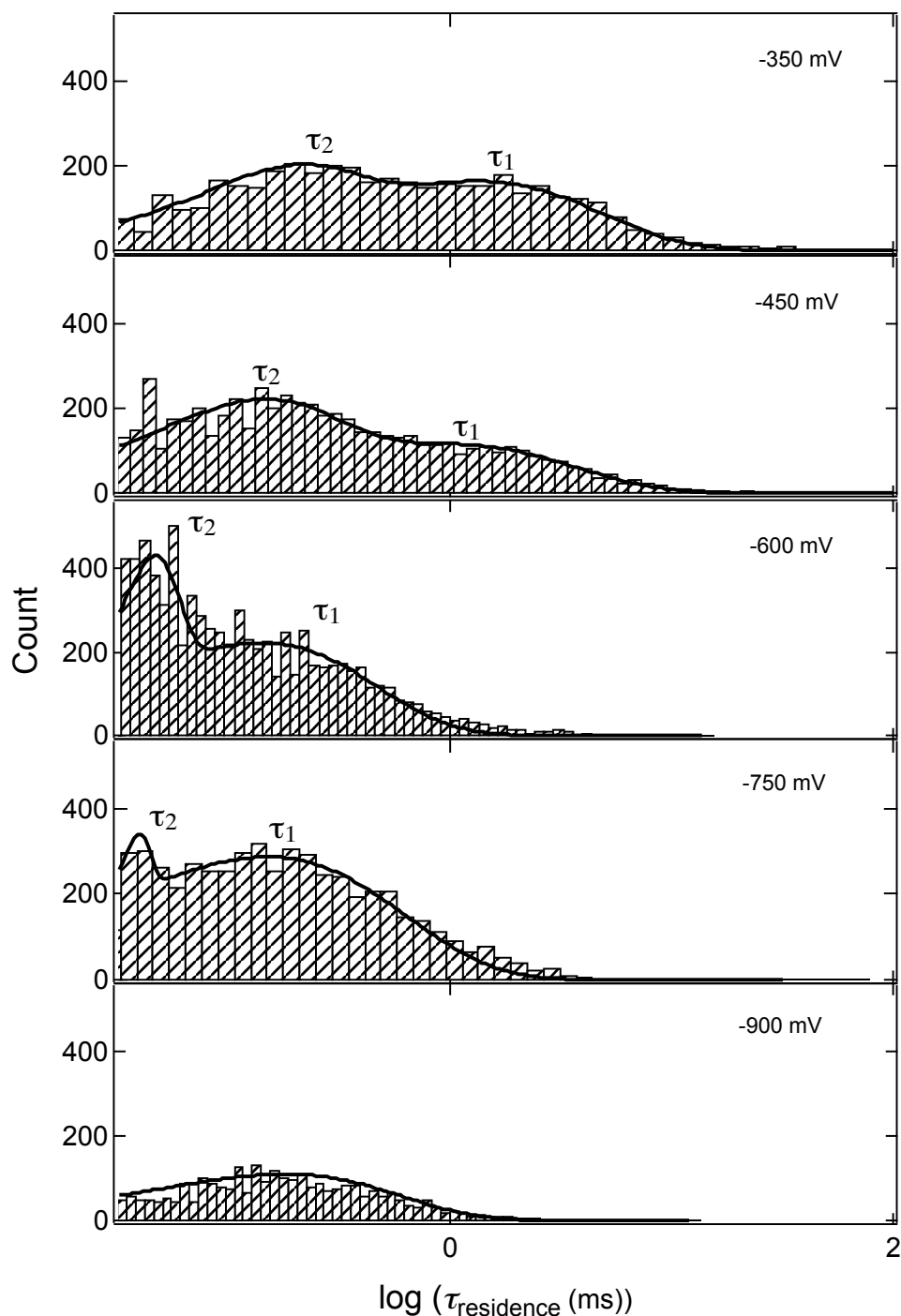
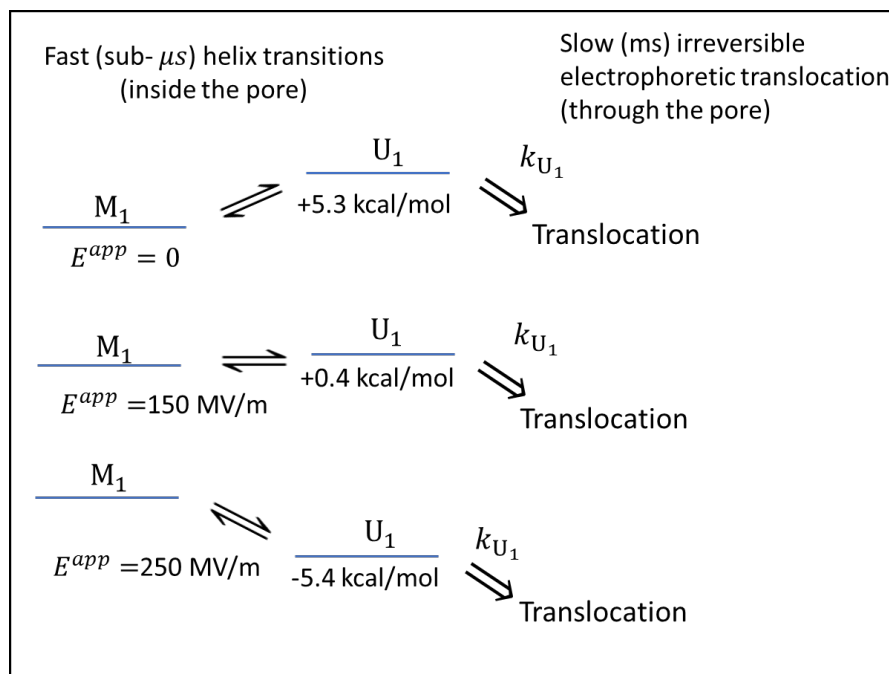


Figure S17. Typical distributions of $\tau_{\text{residence}}$ measured at -350 mV, -450 mV ($M \leftrightarrow U$ regime) and at -600 mV, -750 mV, -900 mV (U regime). The solid curve represents its fit with a bi-modal distribution, yielding two time constants (τ_1 and τ_2) and rates (k_1 and k_2). At -900 mV only a single time constant was observed and attributed to complete linearization of cyt c.

17. Translocation kinetics and fast exchange of folding/unfolding α -helices (2.5 nm pore).

Here we identify the states M, I, and U with the folding of the three main α -helices of cyt c. We consider them to be in rapid exchange as the electric field reduces the free energy gap between the folded and unfolded states of these short (~ 3 turn) α -helices that form an important part of the secondary structure of cyt c. As these states undergo thermodynamic exchange on the sub-microsecond timescale(24-26), the main channel for the translocation within the 2.5 nm pore involves the unfolded U-state. We hypothesize that the folded α -helices block ion current as well as act to retard passage of the protein through the pore, so that the U-state is the primary form of the protein during its passage. Once formed, the various configurations and conformations of the U-state within the pore are pulled by electrophoretic forces through the pore on a much slower timescales than the folding/unfolding transitions of the α -helical segments. These slower translocation timescales, which are associated with the various U-state configurations within the pore, give rise to the distribution of residence times observed on the ms timescale in Fig. S17 and Fig. 3F (insert). In order to enter the pore, a partially unfolded M-state must be formed at the mouth of the pore where the E62 salt bridge has broken and the omega loops have loosened or unfolded, allowing squeezing of the protein into the pore in two separate configurations, which we have labeled as M_1 and M_2 . We have considered two different routes between the M- and U-states. One involves a two-state model (a direct transition from M where all 3 helices unfold to form U) and the other is a three-state model which is sequential(23, 27, 28) and involves formation of an intermediate I-state where one of the α -helices unfolds at lower energies, followed by the other two at higher energy, in a stepwise pathway to the U-state. In order to better visualize the time-scale separation and the role of the electric field in modifying the state energies, the simpler kinetic scheme for the 2-state model is depicted below. In this



example, there are two conformational states (M_1 and U_1) considered in the limit where only the U_1 -state is able to effectively translocate through the pore (i.e., where $k_{M_1} \rightarrow 0$).

Two-state Model

When two-states undergo fast interconversion ($M_1 \rightleftharpoons U_1$) the overall kinetic translocation rate can be written as:

$$k_{tr(M_1 \rightleftharpoons U_1)} = P_{M_1} k_{M_1} + P_{U_1} k_{U_1} \quad (S9)$$

where we take $\Delta\Delta H_{M_1 U_1}^{E_{app}} = -\Delta p_{M_1 U_1} E_{app}$, for simplicity and write the probability of finding cyt c in state U_1 as

$$P_{U_1} = \mathcal{N}^{-1} e^{-\frac{\{\Delta\Delta G_{M_1 U_1} - \Delta p_{M_1 U_1} E_{app}\}}{k_B T_0}} \quad (S10)$$

$$\text{with } \mathcal{N} = \left[1 + e^{-\frac{\{\Delta\Delta G_{M_1 U_1} - \Delta p_{M_1 U_1} E_{app}\}}{k_B T_0}} \right].$$

We let $k_{M_1} \rightarrow 0$ because of its significant α -helical content and then take:

$$k_{U_1} = k_a e^{-\left[\frac{\Delta G_{U_1}^{\ddagger tr} - \beta_{U_1} E_{app}}{k_B T_0} \right]} \equiv k_{0U_1} e^{\frac{\beta_{U_1} E_{app}}{k_B T_0}} \quad (S11)$$

where $-\beta_{U_1} E_{app}$ represents the reduction in the translocation kinetic barrier due to the electrophoretic force (29) that pulls the unfolded protein through the pore. Thus, the translocation rate can be written as:

$$k_{tr(M_1 \leftrightarrow U_1)} = \mathcal{N}^{-1} \left[k_{0U_1} e^{-\frac{\{\Delta\Delta G_{M_1 U_1} - \beta_{U_1}^* E_{app}\}}{k_B T_0}} \right] \quad (S12)$$

$$\text{with } \beta_{U_1}^* = \beta_{U_1} + \Delta p_{M_1 U_1} \text{ and } k_{0U_1} = k_a e^{-\left[\frac{\Delta G_{U_1}^{\ddagger tr}}{k_B T_0} \right]}.$$

Three-state model

For three-state fast exchange translocation kinetics $k_{tr(M_2 \leftrightarrow I \leftrightarrow U_2)} \cong P_I k_I + P_{U_2} k_{U_2}$, so that:

$$k_{tr(M_2 \leftrightarrow I \leftrightarrow U_2)} = \mathcal{N}^{-1} \left[k_{0U_2} e^{-\frac{\{\Delta\Delta G_{M_2 U_2} - \beta_{U_2}^* E_{app}\}}{k_B T_0}} + k_{0I} e^{-\frac{\{\Delta\Delta G_{M_2 I} - \beta_I^* E_{app}\}}{k_B T_0}} \right] \quad (S13)$$

$$\text{with } \mathcal{N} = \left[1 + e^{-\frac{\{\Delta\Delta G_{M_2I} - \Delta p_{M_2I} E_{app}\}}{k_B T_0}} + e^{-\frac{\{\Delta\Delta G_{M_2U_2} - \Delta p_{M_2U_2} E_{app}\}}{k_B T_0}} \right]$$

$$\text{and } \beta_{U_2}^* = \beta_{U_2} + \Delta p_{M_2U_2}, \beta_I^* = \beta_I + \Delta p_{M_2I}.$$

Where, just as for the two-state model, we have defined:

$$k_{U_2} = k_a e^{-\left[\frac{\Delta G_{U_2}^{\ddagger tr} - \beta_{U_2} E_{app}}{k_B T_0}\right]} \equiv k_{0U_2} e^{\frac{\beta_{U_2} E_{app}}{k_B T_0}} \quad \text{and} \quad k_I = k_a e^{-\left[\frac{\Delta G_I^{\ddagger tr} - \beta_I E_{app}}{k_B T_0}\right]} \equiv k_{0I} e^{\frac{\beta_I E_{app}}{k_B T_0}}.$$

Fitting parameters

Using the value of $\Delta\Delta G_{M_1U_1} = 8.9 k_B T_0$ and $\Delta p_{M_1U_1} = 70.2$ Debye ($0.057 \frac{k_B T_0}{MV/m}$) (Table 2 main text), we have 4 unknown parameters k_{0M_1} , k_{0U_1} , β_{M_1} and β_{U_1} to fit the two-state translocation kinetics. Using the extrapolated translocation rates in Fig. 3F of the main text (Sec. 19, Fig. S20, Table S7), we have $\frac{k_{0M}}{k_{0U}} \sim 10^{-5} - 10^{-6}$. Thus, as noted above, we take $\frac{k_{0M}}{k_{0U}} \sim 0$ which leads directly to Eq. S12.

In Fig. S18, we fit the M_1 data with Eq. S12 (two unknown parameters k_{0U_1} and β_{U_1}), which yields $k_{0U_1} = 5839 s^{-1}$ and $\beta_{U_1} = 3.0$ Debye. The value of $\ln k_{0U_1} = 8.67$ also agrees very well with extrapolated translocation rate of state U_1 in Fig. 3F (see Sec. 19, Fig. S20, Table S7). In Fig. S18, we fit the M_1 data with Eq. S13 and use $\Delta\Delta G_{M_2U_2} = 9.1 k_B T_0$ and $\Delta p_{M_2U_2} = 91.4$ Debye ($0.074 \frac{k_B T_0}{MV/m}$) as well as $\Delta\Delta G_{M_2I} = 4.0 k_B T_0$ and $\Delta p_{M_2I} = 44$ Debye ($0.036 \frac{k_B T_0}{MV/m}$) from Table 2 of main text. Thus,

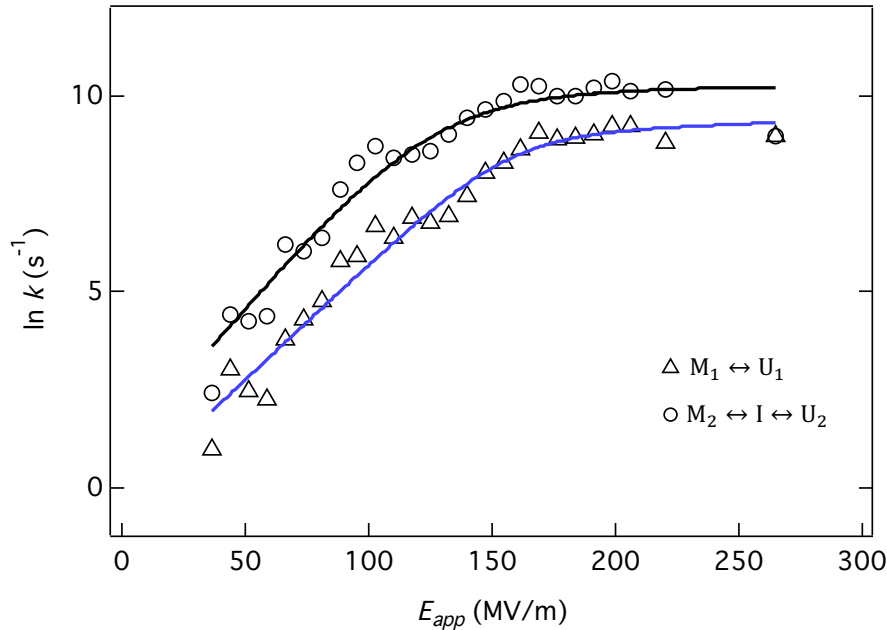


Figure S18. Fit of translocation rates ($d_{pore} = 2.5$ nm, $L = 3.4$ nm) with Eq. S12 (blue curve) for black triangles and fit with Eq. S13 (black curve) for black circle. The parameters obtained from the fit are given Table S6.

we have 4 unknown parameters k_{0I} , k_{0U_2} , β_I and β_{U_2} . The extrapolated translocation rates from Fig. 3F (see Sec. 19, Fig. S20, Table S7) of the main text again justify setting $k_{0M_2} \sim 0$. We fit the black circle data using Eq. S13 which yields $k_{0I} = 72 \text{ s}^{-1}$, $\beta_I = 47.17 \text{ Debye}$ (or $0.038 \frac{k_B T_0}{MV/m}$), $k_{0U_2} = 10712 \text{ s}^{-1}$, and $\beta_{U_2} = 1.75 \text{ Debye}$ (or $0.0014 \frac{k_B T_0}{MV/m}$). The values of $k_{0I} = 72 \text{ s}^{-1}$ ($\ln k_{0I} = 4.28$) is in very close agreement with the translocation rates (extrapolated to zero field) using data in the $M_2 \leftrightarrow I \leftrightarrow U_2$ region of Fig. 3F. Further the value of β_I , which is a measure of the field dependence of the electrophoretic force, is in very close agreement with the slope of translocation rates in $M \leftrightarrow U$ regime. The fit did not converge when we set $k_{0I} = 0$ and tried to fit the data with only k_{0U_2} and β_{U_2} as adjustable parameters.

Table S6: Extracted parameters from the fit of kinetic data (Fig. S18) from Eq. S12 (triangles) and Eq. S13 (circles).

Parameters	$M_1 \leftrightarrow U_1$
k_{0U_1}	5839 s^{-1}
β_{U_1}	3.02 Debye

Parameters	$M_2 \leftrightarrow I \leftrightarrow U_2$
k_{0I}	72 s^{-1}
β_I	47.2 Debye
k_{0U_2}	10712 s^{-1}
β_{U_2}	1.75 Debye

18. Extraction of zero-field translocation barrier of U state for a 2.0 nm pore ($L = 4.1 \text{ nm}$).

To extract the translocation barrier of U-state we used time constant τ_{ii2} of life-time histograms of level ii (left inset Fig. 2B and Fig. 2E). This is because only the time constant of level ii decreases with voltage (Fig. 2F) which is indicative of successful translocation unlike τ_{ii1} which does not change with voltage in this region. The value of $\Delta G_U^{\ddagger tr}$ for the 2nm pore (Fig. S19) is about $2 k_B T_0$ greater than the value $\Delta G_I^{\ddagger tr} \cong 12 k_B T_0$ found for the 2.5 nm pore and at least 2 times greater than $\Delta G_U^{\ddagger tr}$ for 2.5 nm pore (see discussion following Eq. 8 of main text). This, along with the kinetic analysis of translocation rates, strongly suggests that the value of $\Delta G_M^{\ddagger tr}$ for 2nm is likely to be much greater than the unfolding energy barriers (ΔG_{NU}^{\ddagger}) and that squeezing of the metastable M-state into the 2.0 nm pore is kinetically unlikely.

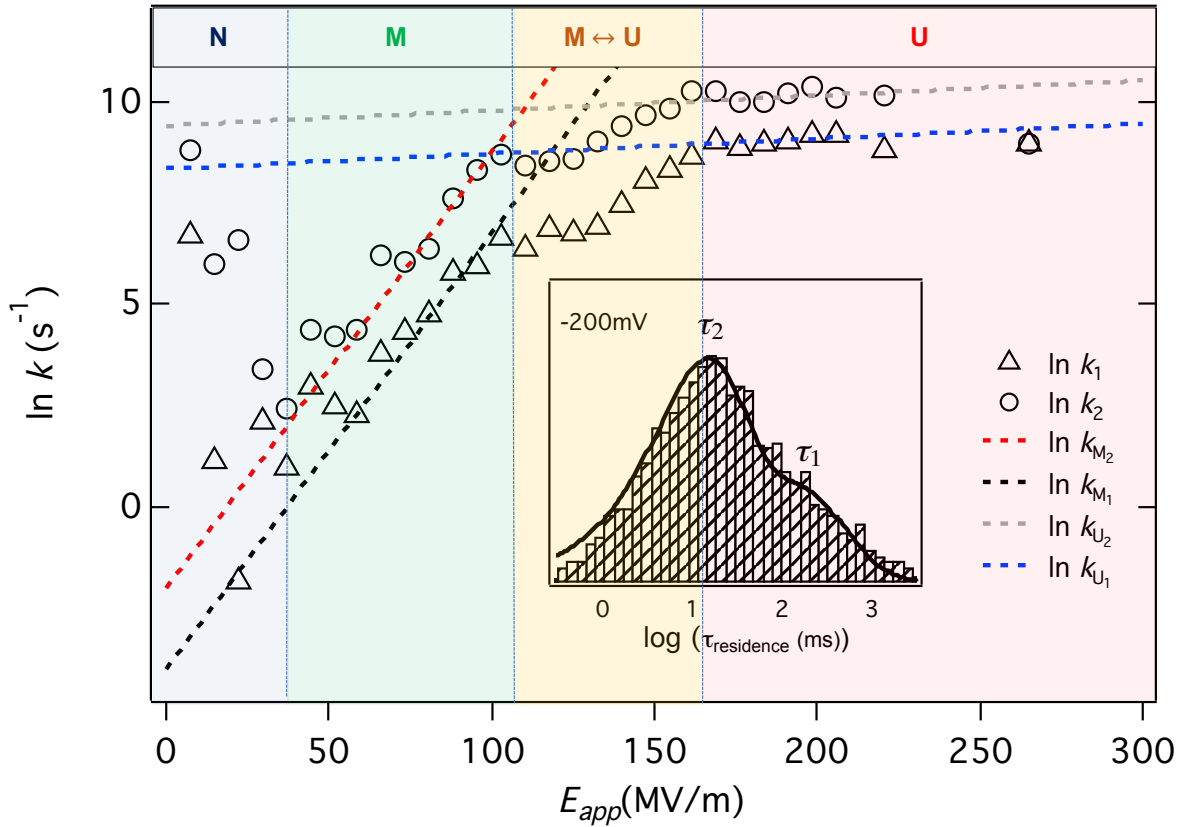


Figure S20. Extrapolation of translocation rates at zero electric-field (2.5 nm pore, $L=3.4$ nm). By extrapolating the rates to zero field with a linear fit of the data (dashed lines), we have evaluated the zero field $\Delta G^{\ddagger tr}$ for each state (see Table S7). Slopes of the dashed lines (which represents electrophoretic force constants or β -values) are 0.11, and 0.004 for the M, and U regimes, respectively (in units of $\frac{k_B T_0}{MV/m}$). In the intermediate M \leftrightarrow U regime, the slope is $\sim 0.04 \frac{k_B T_0}{MV/m}$.

Table S7: Extrapolated translocation rate constants (From Fig. S20) of conformationally excited states (M_1 , M_2 , U_1 , and U_2) of cyt c at zero electric field and the corresponding values of electrophoretic force constant or β -value and $\Delta G^{\ddagger tr}$ (using Eq. 8 of the main text).

States	$\ln[k_0]$ (s^{-1})	β (Debye)	$\Delta G^{\ddagger tr}$ ($k_B T_0$)
M_1	-4	135.9	20.35
M_2	-1.9	135.9	18.25
U_1	8.35	4.9	8
U_2	9.4	4.9	6.95

20. Open pore current vs voltage measurements for different pore diameters.

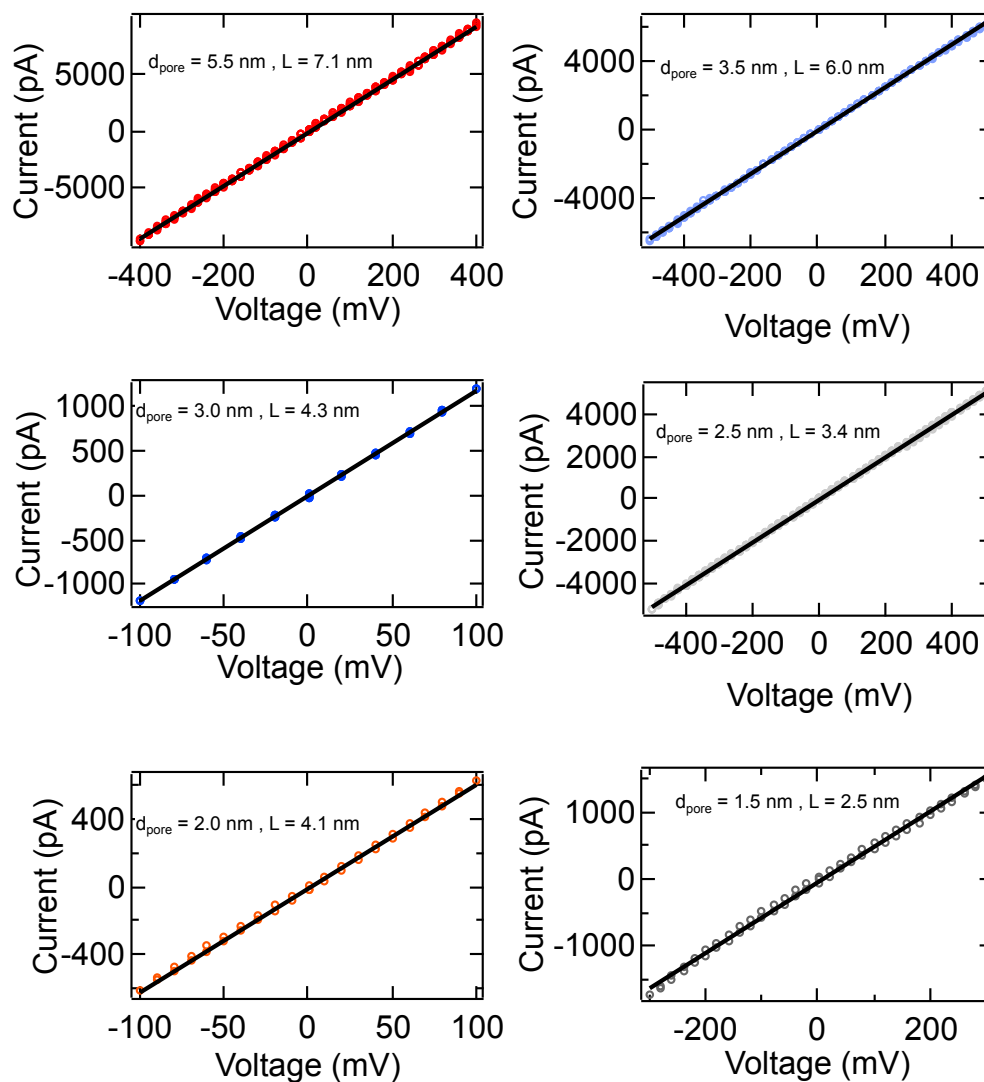


Figure S21. Open-pore (I_o) current vs voltage measurements for different pore diameters employed in this study. The colored circles are the measured open pore currents at a given voltages and dark black lines are the linear fit of the data.

21. Scenarios for level ii event distributions in the 2.0 nm diameter pore

Possible scenarios for the observed event distributions associated with the 2.0 nm pore involve the idea that the two time-constants associated with blockade level ii are related to U-states that thread differently depending on the route taken in their formation. For example, the “direct” U-state formation from $M \rightarrow U$ and the “sequential” formation via $M \rightarrow I \rightarrow U$ may lead to differing behavior upon threading. The observation of two separate time constants (τ_{ii1} and τ_{ii2}) within blockade level ii means there must be at least two states contributing to level ii. Thus, we suggest that the different possible threading states may be associated with “direct” and “sequential” unfolding processes at the pore mouth prior to threading. The longer time constant τ_{ii2} decreases with increasing voltage across the entire range and is therefore consistent with the idea that it corresponds to increased translocation rates of a properly threaded U-state as voltage is increased. The fast time constant ($\tau_{ii1} \sim 0.5$ ms) appears to be independent of voltage below -500 mV, and has a lower current blockade ratio compared to the slow time constant τ_{ii2} (Fig S22). We also observe multiple sequences of the type $i \rightarrow ii \rightarrow \text{open}$ pore, and we rarely observe systematic sequences of the type $i \rightarrow ii \rightarrow i$. This suggests that, after a short-lived attempt at translocation by a partially-threaded state, the protein might escape to the cis chamber where it commences to refold in solution, rather than re-establishing the M-state and the i-level blockade at the pore mouth (the latter scenario is unlikely because it would lead to a $i \rightarrow ii \rightarrow i$ sequence).

A very different scenario, which remains consistent with the observed a $i \rightarrow ii \rightarrow \text{open}$ sequence, is that one of the threaded states (associated with τ_{ii1}) translocates so rapidly into the trans chamber that its weaker voltage dependence cannot be accurately captured because the timescales are close to the limits of our resolution. In this scenario, the slower time constant (τ_{ii2}), with its much stronger voltage dependence, would correspond to threading and translocation of a partially unfolded state that must overcome a voltage dependent barrier of some sort. Because of these very different scenarios, more experiments and further analysis (possibly including even more than two levels) would clearly be needed to fully interpret and understand these interesting results.

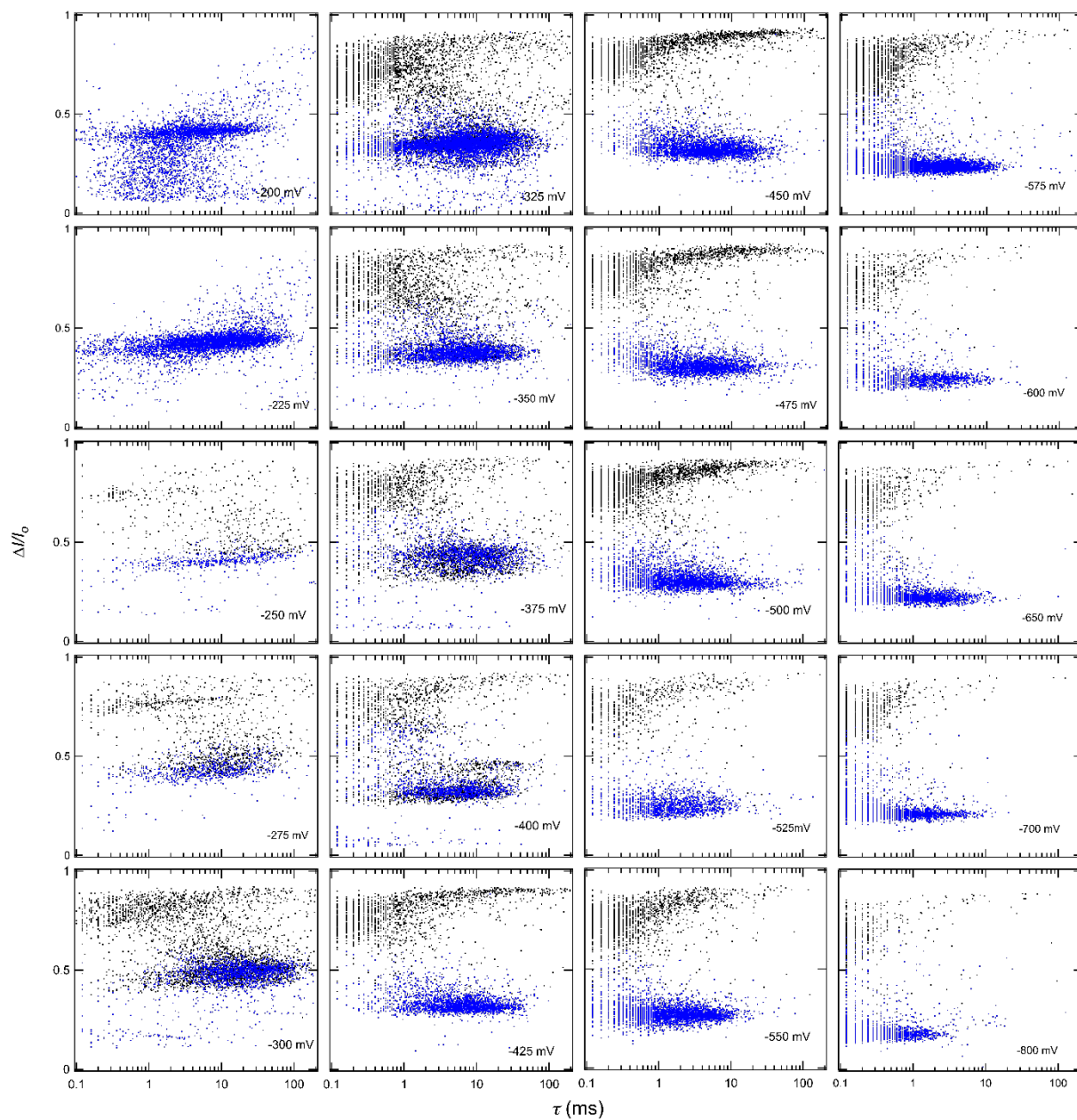


Figure S22. Scatter plots for $\Delta I/I_0$ vs τ for events associated with the 2.0 nm pore experiments at different voltages. Blue dots represents the events associated with level i whereas black dots represent events associated with level ii.

References:

1. M. Wanunu, W. Morrison, Y. Rabin, A. Y. Grosberg, A. Meller, Electrostatic focusing of unlabelled DNA into nanoscale pores using a salt gradient. *Nat. Nanotechnol.* **5**, 160-165 (2010).
2. M. Wanunu *et al.*, Rapid electronic detection of probe-specific microRNAs using thin nanopore sensors. *Nat. Nanotechnol.* **5**, 807-814 (2010).
3. S. Carson, J. Wilson, A. Aksimentiev, M. Wanunu, Smooth DNA transport through a narrowed pore geometry. *Biophys. J.* **107**, 2381-2393 (2014).
4. J. Larkin, R. Y. Henley, M. Muthukumar, J. K. Rosenstein, M. Wanunu, High-bandwidth protein analysis using solid-state nanopores. *Biophys. J.* **106**, 696-704 (2014).
5. P. Waduge *et al.*, Nanopore-Based Measurements of Protein Size, Fluctuations, and Conformational Changes. *ACS Nano* **11**, 5706-5716 (2017).
6. H. Yamazaki *et al.*, Label-Free Single-Molecule Thermoscopy Using a Laser-Heated Nanopore. *Nano Lett.* **17**, 7067-7074 (2017).
7. S. W. Kowalczyk, A. Y. Grosberg, Y. Rabin, C. Dekker, Modeling the conductance and DNA blockade of solid-state nanopores. *Nanotechnology* **22**, 315101 (2011).
8. W. H. Koppenol, J. D. Rush, J. D. Mills, E. Margoliash, The dipole moment of cytochrome c. *Mol. Biol. and Evol.* **8**, 545-558 (1991).
9. W. Humphrey, A. Dalke, K. Schulten, VMD: Visual molecular dynamics. *J. Mol. Graph.* **14**, 33-38 (1996).
10. G. W. Bushnell, G. V. Louie, G. D. Brayer, High-resolution three-dimensional structure of horse heart cytochrome c. *J. Mol. Biol.* **214**, 585-595 (1990).
11. W. L. Jorgensen, J. Chandrasekhar, J. D. Madura, R. W. Impey, M. L. Klein, Comparison of simple potential functions for simulating liquid water. *J. Chem. Phys.* **79**, 926-935 (1983).
12. J. C. Phillips *et al.*, Scalable molecular dynamics on CPU and GPU architectures with NAMD. *J. Chem. Phys.* **153**, 044130 (2020).
13. A. D. MacKerell *et al.*, All-atom empirical potential for molecular modeling and dynamics studies of proteins. *J. Phys. Chem. B* **102**, 3586-3616 (1998).
14. J. Comer, V. Dimitrov, Q. Zhao, G. Timp, A. Aksimentiev, Microscopic Mechanics of Hairpin DNA Translocation through Synthetic Nanopores. *Biophys. J.* **96**, 593-608 (2009).
15. U. Essmann *et al.*, A smooth particle mesh Ewald method. *J. Chem. Phys.* **103**, 8577-8593 (1995).
16. G. J. Martyna, D. J. Tobias, M. L. Klein, Constant pressure molecular dynamics algorithms. *J. Chem. Phys.* **101**, 4177-4189 (1994).
17. H. J. C. Berendsen, J. P. M. Postma, W. F. van Gunsteren, A. DiNola, J. R. Haak, Molecular dynamics with coupling to an external bath. *J. Chem. Phys.* **81**, 3684-3690 (1984).
18. D. B. Wells, V. Abramkina, A. Aksimentiev, Exploring transmembrane transport through α -hemolysin with grid-steered molecular dynamics. *J. Chem. Phys.* **127**, 125101 (2007).
19. A. Aksimentiev, K. Schulten, Imaging α -Hemolysin with Molecular Dynamics: Ionic Conductance, Osmotic Permeability, and the Electrostatic Potential Map. *Biophys. J.* **88**, 3745-3761 (2005).
20. J. Wilson, K. Sarthak, W. Si, L. Gao, A. Aksimentiev, Rapid and Accurate Determination of Nanopore Ionic Current Using a Steric Exclusion Model. *ACS Sens.* **4**, 634-644 (2019).

21. M. P. Eastwood, C. Hardin, Z. Luthey-Schulten, P. G. Wolynes, Evaluating protein structure-prediction schemes using energy landscape theory. *IBM J. Res. Dev.* **45**, 475-497 (2001).
22. C. G. Rodrigues, D. C. Machado, S. F. Chevtchenko, O. V. Krasilnikov, Mechanism of KCl enhancement in detection of nonionic polymers by nanopore sensors. *Biophys. J.* **95**, 5186-5192 (2008).
23. W. Hu, Z. Y. Kan, L. Mayne, S. W. Englander, Cytochrome c folds through foldon-dependent native-like intermediates in an ordered pathway. *Proc. Natl. Acad. Sci. U.S.A.* **113**, 3809-3814 (2016).
24. J. A. Ihalainen *et al.*, α -Helix folding in the presence of structural constraints. *Proc. Natl. Acad. Sci. U.S.A.* **105**, 9588 (2008).
25. J. H. Werner, R. B. Dyer, R. M. Fesinmeyer, N. H. Andersen, Dynamics of the Primary Processes of Protein Folding: Helix Nucleation. *J. Phys. Chem. B* **106**, 487-494 (2002).
26. E. A. Gooding *et al.*, The effects of individual amino acids on the fast folding dynamics of α -helical peptides. *Chem. Comm.* 10.1039/B511072F, 5985-5987 (2005).
27. M. M. Krishna, Y. Lin, J. N. Rumbley, S. W. Englander, Cooperative omega loops in cytochrome c: role in folding and function. *J. Mol. Biol.* **331**, 29-36 (2003).
28. H. Maity, M. Maity, S. W. Englander, How cytochrome c folds, and why: submolecular foldon units and their stepwise sequential stabilization. *J. Mol. Biol.* **343**, 223-233 (2004).
29. S. van Dorp, U. F. Keyser, N. H. Dekker, C. Dekker, S. G. Lemay, Origin of the electrophoretic force on DNA in solid-state nanopores. *Nat. Phys.* **5**, 347-351 (2009).